Cerebral Cortex, February 2016;26: 855–872

doi: 10.1093/cercor/bhv271
Advance Access Publication Date: 18 November 2015
Original Article

ORIGINAL ARTICLE

Developmental Profile, Morphology, and Synaptic Connectivity of Cajal–Retzius Cells in the Postnatal Mouse Hippocampus

Max Anstötz[1,3], Hao Huang[2], Ivan Marchionni[2,6], Iris Haumann[3], Gianmaria Maccaferri[2,†] and Joachim H.R. Lübke[1,4,5,†]

[1]Institute of Neuroscience and Medicine INM-2, Research Centre Jülich GmbH, Jülich 52425, Germany, [2]Department of Physiology, Northwestern University, Feinberg School of Medicine, IL 60611-3008, USA, [3]Institute for Neuroanatomy, University/University Hospital Hamburg, Hamburg 20246, Germany, [4]Department of Psychiatry, Psychotherapy and Psychosomatics, RWTH/University Hospital Aachen, Aachen 52074, Germany, [5]JARA Translational Medicine, Jülich/Aachen, Germany and [6]Current address: Instituto Italiano di Tecnologia, Neuroscience and Brain Technologies, Genova 16163, Italy

Address correspondence to Joachim H.R. Lübke, Institute for Neuroscience and Medicine INM-2, Research Centre Jülich GmbH, 52425 Jülich, Germany. Email: j.luebke@fz-juelich.de; Gianmaria Maccaferri, Department of Physiology, Feinberg School of Medicine Northwestern University, Chicago, IL 60611, USA. Email: g-maccaferri@northwestern.edu; Max Anstötz, University Medical Center Hamburg-Eppendorf, Institute of Neuroanatomy, 20245 Hamburg, Germany. Email: m.anstoetz@uke.de

[†]Both authors equally share senior authorship.

Abstract

Cajal–Retzius (CR) cells are early generated neurons, involved in the assembly of developing neocortical and hippocampal circuits. However, their roles in networks of the postnatal brain remain poorly understood. In order to get insights into these latter functions, we have studied their morphological and synaptic properties in the postnatal hippocampus of the CXCR4-EGFP mouse, where CR cells are easily identifiable. Our data indicate that CR cells are nonuniformly distributed along different subfields of the hippocampal formation, and that their postnatal decline is regulated in a region-specific manner. In fact, CR cells persist in distinct areas of fully mature animals. Subclasses of CR cells project and target either local (molecular layers) or distant regions [subicular complex and entorhinal cortex (EC)] of the hippocampal formation, but have similar firing patterns. Lastly, CR cells are biased toward targeting dendritic shafts compared with spines, and produce large-amplitude glutamatergic unitary postsynaptic potentials on γ-aminobutyric acid (GABA) containing interneurons. Taken together, our results suggest that CR cells are involved in a novel excitatory loop of the postnatal hippocampal formation, which potentially contributes to shaping the flow of information between the hippocampus, parahippocampal regions and entorhinal cortex, and to the low seizure threshold of these brain areas.

Key words: CXCR4-EGFP mice, hippocampal Cajal–Retzius cells, light- and electron microscopy, patch-clamp recordings, synaptic connectivity

Introduction

Cajal–Retzius (CR) cells are early born neurons that populate the marginal zone of the developing neocortex and hippocampus (for review, see Soriano and Del Río 2005). At early stages, CR cells have been highlighted as the main cellular source of the glycoprotein reelin (D'Arcangelo et al. 1995; Ogawa et al. 1995; Derer et al. 2001; but see Alcántara et al. 1998; Pesold et al. 1998, 1999 for reelin expression in γ-aminobutyric acid-ergic (GABAergic) interneurons of the postnatal cortex), which is essential for establishing the correct architecture of neocortical and hippocampal circuits (D'Arcangelo et al. 1995; Del Río et al. 1997; Supèr et al. 1998; Ceranik et al. 2000; see also Frotscher 1998). Although various articles have reported the persistence of CR cells in the postnatal hippocampus of several species at more mature stages (rats: Drakew et al. 1998; mice: Alcántara et al. 1998; Supèr et al. 1998; pigs: Abraham et al. 2004; humans: Abraham and Meyer 2003), a detailed analysis of their fate is still missing, and the signals encoded by their synaptic connections remain unclear.

Recent physiological data have shown that mouse CR cells of the postnatal hippocampus are integrated in local networks via GABAergic synaptic input from specific interneurons (neurogliaform and O-LM cells, Quattrocolo and Maccaferri 2013) and that their optogenetic stimulation activates α-amino-3-hydroxy-5-methyl-4-isoxazolepropionic acid (AMPA)- and N-methyl-d-aspartate (NMDA)-type glutamate receptors both on GABAergic interneurons and CA1 pyramidal cells (Quattrocolo and Maccaferri 2014).

However, structural data have also suggested that CR cells project to distant regions and contribute to the bidirectional synaptic dialog between the hippocampus and the entorhinal cortex (EC) (Ceranik et al. 1999). Although the issue of the synaptic input–output relationship of CR cells with local and distant networks is essential to understand their functions in the developing and mature hippocampus, several key points remain unresolved.

First, neither the spatial distribution nor the postnatal persistence of CR cells of the hippocampal formation has yet been studied quantitatively. Second, it is still unclear whether hippocampal CR cells constitute a structurally homogenous population of neurons and all participate in both local and long-range circuits. In fact, it is now established that CR cells arise from discrete areas in the telencephalon (Takiguchi-Hayashi et al. 2004; Bielle et al. 2005; Yoshida et al. 2006; Gu et al. 2009, 2011; Tissir et al. 2009) and colonize the developing marginal zone, which will later develop into the outer molecular layer of the dentate gyrus (OML) and stratum lacunosum-moleculare (SLM), or layer 1 (L_1) in other cortices. Although neocortical CR cells of different ontogenetic origin appear homogenous in their basic structure and electrophysiological properties (Sava et al. 2010), nothing is known, currently, about the homogeneity/heterogeneity of hippocampal CR cells with respect to their local/long-range synaptic connectivity. Third, the ultrastructure of the postsynaptic target domains of hippocampal CR cells remains elusive. Thus, the main target structures of CR cell axons remain to be identified. Lastly, although the optogenetic stimulation of CR cells may trigger firing in postsynaptic GABAergic interneurons (Quattrocolo and Maccaferri 2014), the strength of their unitary excitatory postsynaptic potentials (uEPSPs) remains unknown. This is important to establish whether CR cell-dependent control of GABAergic input onto pyramidal cells requires the synchronous activity of a large versus a small number of presynaptic neurons.

Here we have taken advantage of a reporter mouse expressing enhanced green fluorescent protein (EGFP) in hippocampal CR cells, the CXCR4-EGFP mouse (Marchionni et al. 2010; Anstötz et al. 2014), to directly address these issues.

Materials and Methods

All experimental procedures described here were performed in accordance with the National Institute of Health (NIH) guidelines for the Care and Use of Laboratory Animals, following Northwestern University Institutional Animal Care and Use Committee (IACUC), by the Animal Research Committee of the Research Centre Jülich GmbH and approved protocols and complied with the guidelines laid out in the EU directive regarding the protection of animals used for experimental and scientific purposes.

Fluorescence Microscopy

To analyze the density and distribution pattern of CR cells in the hippocampal formation we took advantage of the CXCR4-EGFP reporter mouse where these neurons were fluorescently labeled and thus easily detectable (see Marchionni et al. 2010; Anstötz et al. 2014). CXCR4-EGFP mice ($n = 25$) aged postnatal day (P) 8 to P60 were deeply anesthetized using isoflurane (3–4% in air). The level of anesthesia was assessed by monitoring the pedal withdrawal reflex, and by pinching the tail or ear. Following deep anesthesia, mice were perfusion-fixed through the heart using 4% phosphate-buffered paraformaldehyde (0.1 M PB, pH 7.4). After fixation, brains were removed from the skull and post-fixed in the same, but fresh fixative overnight at 4°C. Brains were then cut in the horizontal plane at a thickness of 50 µm with a vibratome (Leica VT 1000, Leica Microsystems, Nussloch, Germany), collected in 0.1 M PB and finally embedded in water-based Moviol (Hoechst AG, Frankfurt AM, Germany) on glass slides.

Fluorescence microscopic images were obtained with an Olympus BX61 (Olympus, Hamburg, Germany) and a Kyence BX-9000. For Extended Focal Imaging multiple Z-stacks were obtained and in-focus areas merged in Adobe Photoshop®.

Confocal microscopy images were captured using a Leica SP5 with HyD detectors. Single- or multichannel fluorescence images were saved individually for analysis and merged together for co-localization studies and figures using Adobe Photoshop®. Final figures were made using Adobe Illustrator®.

Electrophysiology and Biocytin-Filling

Slice Preparation

CXCR4-EGFP mice pups aged P6–P21 ($n = 30$) were deeply anesthetized using isoflurane, decapitated and the brain was quickly extracted. Transverse hippocampal slices (350–400 µm in thickness) were prepared using methods similar to the ones described by Anstötz et al. (2014). Slices were cut in ice-cold "cutting" artificial cerebrospinal fluid (ACSF) using a Leica VT 1000 vibratome. The composition of the ACSF was (in mM): 130 NaCl, 24 $NaHCO_3$, 3.5 KCl, 1.25 NaH_2PO_4, 1 $CaCl_2$, 2 $MgCl_2$, 10 glucose saturated with 95% O_2–5% CO_2 at pH 7.4. After their preparation, slices were transferred to a storage chamber at 30–33°C for at least 30 min and then allowed to return to room temperature before use. During recordings, slices were superfused by "recording" ACSF of the following composition (in mM): 130 NaCl, 24 $NaHCO_3$, 3.5 KCl, 1.25 NaH_2PO_4, 2 $CaCl_2$, 1 $MgCl_2$, 10 glucose saturated with 95% O_2–5% CO_2 at pH 7.4.

Visual Identification of CR Cells in the Hippocampus

Slices were observed in the recording chamber under an upright microscope (Olympus, Japan). Fluorescence of EGFP-expressing CR cells was excited by an X-Cite Series 120 light source (Exfo, Ontario, Canada) and visualized using a VE1000 camera (DAGE MTI,

Michigan City, IN, USA). Hippocampal CR cells in the SLM or OML of the dentate gyrus were visually identified at ×600 magnification first by fluorescence imaging and subsequently by infrared-differential interference contrast microscopy by their location, the size and shape of their somata and the appearance of a thick stem dendrite originating from one pole of the soma.

Electrophysiological Recordings and Data Analysis

Pipettes were pulled from borosilicate thin glass capillaries with a final resistance of ~3–5 MΩ, filled with filtered intracellular solution of the following composition (in mM): 105 K-methylsulfate, 10 NaCl, 20 KCl, 4 ATP-Mg, 0.3 GTP-Na_3, 16 $KHCO_3$ equilibrated with 95% O_2–5% CO_2 at pH 7.3. For subsequent morphological analysis, 1 mg/ml biocytin (Sigma-Aldrich, New York, USA) was added routinely to the internal solution.

During recording and biocytin-filling (~15–20 min) the membrane properties and firing characteristics of CR cells were examined in the voltage- and current-clamp configuration. Recordings were carried out using a Multiclamp 700B amplifier (Molecular Devices, Sunnyvale, CA, USA). Series resistances were balanced via a bridge circuit in current-clamp mode. Data were filtered at 3 kHz and digitized at 10–20 kHz using a Digidata A/D board and the Clampex 9 program suite (Molecular Devices). All recordings and measurements were carried out at 29–31°C.

Paired Recordings

Simultaneous recordings from presynaptic CR cells and postsynaptic GABAergic interneurons were performed to test for functional connectivity in ($n = 146$) double recordings in slices obtained from P11–P23 CXCR4-EGFP mice. Interneurons were initially distinguished from CR cells in the living slice by their lack of EGFP expression (Quattrocolo and Maccaferri 2013), by larger somata and presence of multiple dendrites originating from the soma. Current steps of brief duration (5 ms) and sufficient amplitude to trigger action potentials were injected in the CR cell at a 100-ms interval to evaluate paired-pulse plasticity. This protocol was repeated every 10 s. Postsynaptic responses were averaged after being aligned on the presynaptic spikes (Marchionni and Maccaferri 2009) to correct the effect of action potential jitter. Averaged postsynaptic responses (from ~20 traces) were obtained and analyzed from 5 connected pairs. General properties of the postsynaptic response (peak amplitude, 20–80% rise time, and 100–37% decay time, paired-pulse ratio) were estimated using the Clampfit program (Molecular Devices). Values are presented as mean ± SE.

Biocytin-Filling and Histological Procedures

During single and paired recordings CR cells and their prospective target neurons were filled with biocytin (~15 min) to reveal their morphology. Slices were fixed in a 0.1 M PB (pH 7.4) solution containing either 4% paraformaldehyde (for light microscopy, LM) or 4% paraformaldehyde and 0.1% glutaraldehyde (for electron microscopy, EM) at 4°C for at least 24 h. They were then either processed for LM- and/or EM as described earlier (Anstötz et al. 2014). In brief, after incubation in ABC-Elite solution (Sigma-Aldrich, Germany) overnight, slices were preincubated in 3′3-diaminobenzidine (DAB; Sigma-Aldrich) and visualized by adding 0.025% H_2O_2 to the DAB solution. The reaction was stopped when dendritic and axonal processes were clearly visible under LM examination. After several washing steps in 0.1 M PB and brief postfixation in osmium tetroxide (1–2 min), sections were embedded in Moviol (Hoechst AG, Frankfurt AM, Germany) and coverslipped for LM. For EM, slices were longer osmicated (0.5% OsO_4 in 0.1 M PB; 30 min), dehydrated in an ascending series of ethanol, followed by propylene oxide (2×, 2 min each), 2 mixtures of propylene oxide and Durcupan (2:1 and 1:1, 1hr each) and then transferred to pure resin overnight. The next day slices were finally flat-embedded in fresh Durcupan (Fluka, Neu-Ulm, Germany) and polymerized at 6°C for 2 days.

Selected blocks containing biocytin-filled CR cells ($n = 6$) were trimmed and ultrathin sections (thickness 50 ± 5 nm, silver to light gray interference contrast) were cut through the dendritic and axonal domain using an ultramicrotome (Leitz Ultracut, Hamburg, Germany). Ultrathin sections were counterstained with uranylacetate (10–15 min) and lead citrate (3–5 min) according to Reynolds (1963) and examined with a Zeiss Libra 120 EM (Fa. Zeiss, Oberkochen, Germany) equipped with a bottom-mounted Proscan 2 K digital camera and the SIS Analysis software. Images were taken at different magnifications and further processed using Adobe Photoshop® and Adobe Illustrator® software packages.

Morphological Reconstructions and Analysis of Biocytin-Filled Hippocampal CR Cells

Only neurons that had no obvious truncation of their dendritic and axonal profiles were used for qualitative and quantitative analysis of their morphology ($n = 63$). Neurons were photographed at various magnifications (Olympus BX61 microscope equipped with fluorescence and SIS Analysis software) to document their dendritic morphology and axonal projection pattern. All cells matching the selective criteria were reconstructed using the NEUROLUCIDA software (MicroBrightfield Europe; Magdeburg, Germany) equipped to an Olympus BX61 microscope. These reconstructions provided the basis for further quantitative morphological analysis of the following parameters: (1) total length of axonal collaterals; (2) maximal horizontal field span of axonal collaterals; (3) axonal endings (following the NEUROLUCIDA software terminology to define terminal points); (4) total length of the dendritic tree; (5) dendritic endings and (6) horizontal soma diameter (pole-to-pole). The field span was corrected for curvature using the borders of the dentate gyrus as a reference. For all data, means ± standard deviation (SD), maximum and minimum values are given. Statistics were performed using IBM SPSS Statistics Ver. 22 (IBM Corp, Armonk, USA).

Axonal and Dendritic Polar Plots and Density Maps

The values for polar plots were generated from the NEUROLUCIDA reconstructions of individual hippocampal CR cells using the NEUROEXPLORER software (MicroBrightfield Europe; Magdeburg, Germany). All neurons were aligned such that the hippocampal fissure was upward. From these values, a normalized average polar plot was obtained for the dendritic and axonal domains. The plots were then generated using Adobe Illustrator®.

In addition, 2-dimensional (2D) maps of dendritic and axonal "segment-length density" were constructed using the computerized 2D reconstructions (for details, see Anstötz et al. 2014). For proper alignment of the cell-type specific density all reconstructed CR cells were projected in a 2D plane and centered to their axonal initial segment. For the "region-specific density" plots cells were aligned into a scheme of a hippocampal slice (horizontal plane) with respect to the relative soma and arborization position. Then axonal and dendritic segment-length was measured in a 50 × 50 µm Cartesian grid, yielding into a raw

density map. The data of "region-specific density" plots were normalized using the average, region-specific CR cell densities of 25 slices. Continuous 2D density functions were constructed using bicubic interpolation in Mathematica 7 (Wolfram Research, Champaign, IL, USA).

Quantification of CR Cell Density and Distribution

CXCR4-EGFP mice aged P8-P60 were prepared as described above ($n = 3$ per age). All quantifications are based on 50-µm thick horizontal slices ($n = 8$ per mouse and age, as described above). Between different brains and ages the same level of the hippocampal formation was used for comparison.

For analysis, z-stacks with 5-µm interval were taken using a Kyence BX-9000 microscope equipped with a Nikon Apo 20 × 0.75NA lens. Each z-stack was analyzed individually using NEUROLUCIDA such that all CR cells were marked and layer borders outlined. For the region-specific counts, 3 regions of interest were defined: the area along the hippocampal fissure (HF) covering both the OML and SLM, the pial surface of L_1 in the subicular complex/EC and pial surface of the dentate gyrus (OML_{ip}).

Cell density was calculated for each region according to the same number of bins in every slice (6 bins for the HF region, 3 for the OML_{ip}, and 2 for L_1).

Conversion of EGFP Into an Electron Dense Reaction Product

To investigate the EGFP-labeled CR cells at the EM level, EGFP was converted into a stable electron dense DAB-reaction product. Four CXCR4-EGFP mice aged P18–24 were deeply anesthetized with Narkodorm® (60 mg/kg body weight) and transcardially perfused as already described above. Vibratome sections (100 µm in thickness) in the horizontal plane were subsequently cryoprotected in 0.1 M PB-buffered 10% and 20% sucrose for 1 h and transferred and stored overnight in PB-buffered 30% sucrose at 4°C. Section were freeze thawed in liquid nitrogen and after several washing steps in 0.1 M PB blocked in 1% bovine serum albumin (BSA) in 0.1 M PB for 2 h. This was followed by incubation in the primary rabbit monoclonal antibody anti-GFP (1:300; Millipore, Hamburg, Germany) diluted in 0.1 M PB containing 0.1% BSA overnight at 4°C. After several washing steps in 0.1 M PB sections were transferred into the secondary antibody, biotinylated anti-rabbit for the detection of the EGFP (1:200; Vector Lab., Darlingham, USA) diluted in 0.1 M PB containing 0.1% BSA for 2 h at room temperature. After several brief washing steps in 0.1 M PB sections were transferred to 0.05 M Tris-buffered saline (TBS; pH 7.4) and incubated in ABC-Elite for 2 h. For the detection of EGFP-labeled CR cells they were reacted in DAB (0.5 mg/mL diluted in 0.05 M TBS) and 0.03% H_20_2 for 15 min in the dark. The reaction was stopped in 0.05 M TBS. After osmium treatment (0.5% in sucrose-buffered 0.1 M PB for 15–30 min) sections were further processed for EM and analyzed as already described above.

Reelin, vGlut, and vGAT Immunohistochemistry

The anesthesia and perfusion of the animals ($n = 10$) was done as already described above. The immunohistochemistry was carried out on free-floating 50-µm thick vibratome sections. After several brief rinses in 1× TBS containing 1% Triton-X 100 (TBST), sections were transferred into 70% formic acid (diluted in double-distilled water for 5 min) and subsequently washed 3 times in 1× TBST. Then sections were preincubated in PBS containing 10% NGS/0.5% Triton X-100 for 1 h. After several brief washing steps, sections were incubated with the primary antibodies: mouse anti-reelin G10 1:400 (Abcam, Cambridge, UK), rabbit anti-vGluT1, rabbit anti-vGluT2, rabbit anti vGAT 1:800 each (SynapticSystems, Göttingen, Germany), rabbit anti-cleaved caspase 3 (Cell Signalling, Frankfurt/M, Germany) diluted in 1% BSA/TBST overnight at 4°C. After several brief washing steps in 1× TBST (1 min each) sections were incubated in the secondary antibody Alexa 568 goat anti-rabbit or Alexa 633 goat anti-mouse 1:800 each (Invitrogen, Darmstadt, Germany) diluted in 1% BSA/TBST for 2 h in the dark. Finally, sections were washed several times in 1% TBST, counterstained with 4′,6-Diamidin-2-phenylindol (DAPI; 1:10000 diluted in PBS), mounted on glass slides, embedded in Moviol and coverslipped. Sections were examined and documented using a Kyence BX-9000 and Leica SP5 microscope.

Results

Density, Distribution Pattern, and General Features of EGFP-Expressing Hippocampal CR Cells

The density and distribution pattern of CR cells were analyzed in horizontal sections through the hippocampal formation using CXCR4-EGFP mice ranging between postnatal days (P) 8–P60. Here, CR cells are fluorescently labeled and thus easily identifiable (Fig. 1*A*). In fact, within both the hippocampal SLM and the OML of the dentate gyrus, EGFP expression is confined exclusively to CR cells (Fig. 1*A*, *B1–B3*, *C*; see also Marchionni et al. 2010; Quattrocolo and Maccaferri 2013). Therefore, despite the presence of EGFP in the dentate gyrus (reflecting the expression of CXCR4 on the membrane of neural stem cells and in their progeny; see Bhattacharyya et al. 2008), and in stratum oriens (SO) and stratum radiatum (SR) of the hippocampus proper, the CXCR4-EGFP mouse is a very useful tool to investigate the localization, density, and distribution of hippocampal CR cells throughout postnatal development.

In addition to their EGFP expression, CR cells appearing structurally healthy (i.e., without signs of degeneration), were always immunopositive for reelin ($n = 543$, Fig. 1*C*), although this protein was also found in GABAergic interneurons of the SLM and OML (Fig. 1*C*).

In general, CR cells were heterogeneously distributed through the hippocampal formation (Figs 1*A*, *B1–B3*, 2*A*,*B*). Based on their locations, we distinguished 3 classes of CR cells (Fig. 2*A*) as belonging to: (1) the region along the HF covering both SLM and the OML of the dentate gyrus, (2) the OML_{ip} of the dentate gyrus and (3) L_1 of the subicular complex and (occasionally) EC. Overall, the highest densities were observed along the HF (10.7 ± 0.3 cells per 5000 µm^2 at P15, in particular close to the pole region, see Fig. 2*B*). Lower densities were observed in the OML_{ip} and L_1 (2.6 ± 0.2 cells per 5000 µm^2 and 3.7 ± 0.4 cells per 5000 µm^2, respectively, $n = 3$ animals).

The Developmental-Dependent Decline of CR Cell Numbers is Region-specific

A possible explanation for the observed difference is that CR cell density could also depend on the presence of nonuniform, region-specific, developmental processes. The number of neocortical CR cells declines dramatically around P14 and appears to be regulated by caspase-3-dependent apoptotic processes (Chowdhury et al. 2010; Anstötz et al. 2014). When we quantified CR cell densities in animals of different postnatal ages (P8–P60, Fig. 3A1-A2, *B*), consistently the highest values were found along the HF region, when compared with the OML_{ip} and L_1. In addition, CR cells of

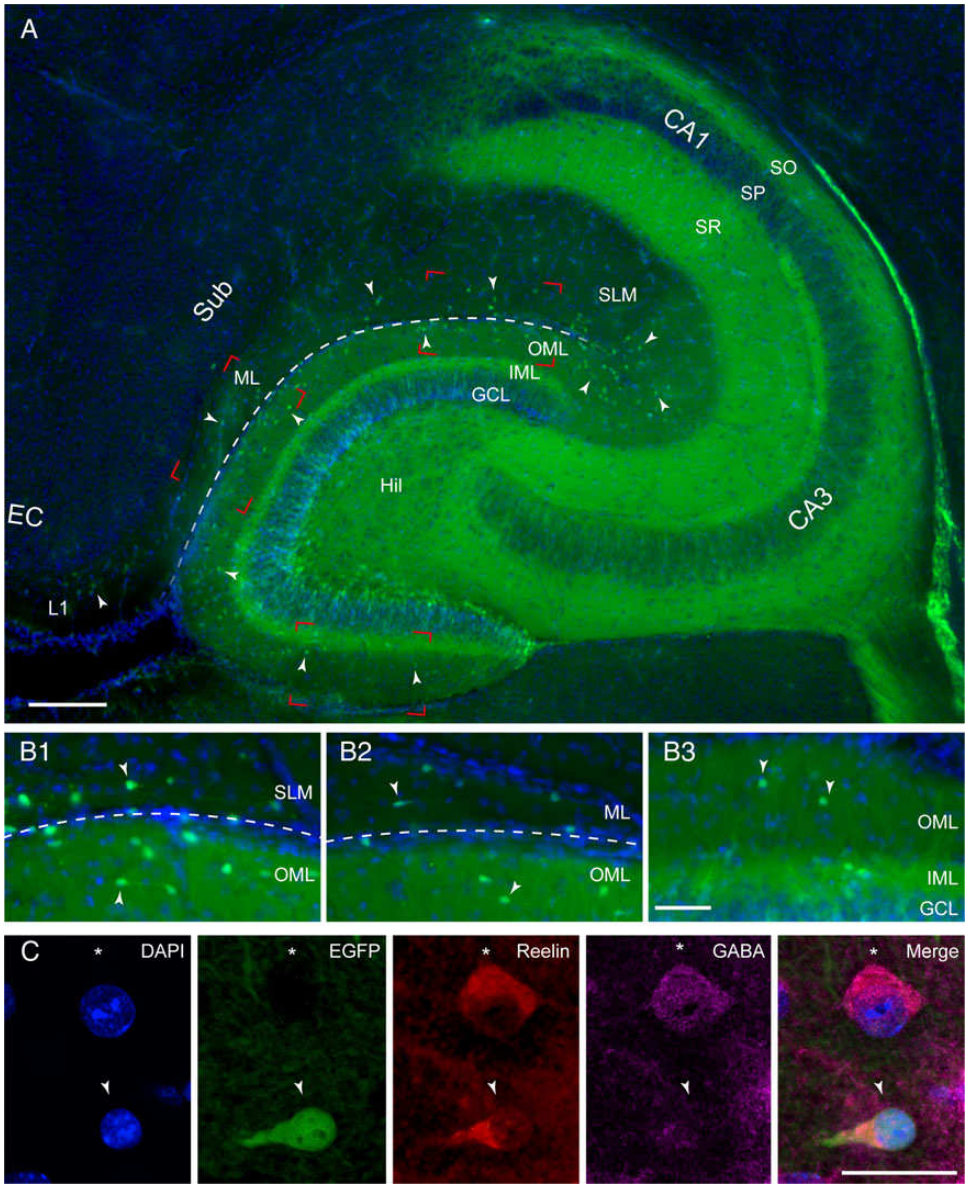

Figure 1. Distribution of CR cells in the hippocampal formation. (*A*) Low-power fluorescent microscopic image showing the distribution of EGFP expressing CR cells in a horizontal brain slice of a P18 mouse hippocampus (blue: DAPI counterstaining). EGFP-positive CR cells are located throughout the entire OML and SLM as indicated by the white arrowheads. The hippocampal fissure is marked by the dashed line. Note the auto-fluorescence for the GFP spectrum within the stratum oriens (SO), stratum pyramidale (SP), stratum radiatum (SR), inner molecular layer (IML), granule cell layer (GCL), and hilus (Hil). Further abbreviations for hippocampal subregions: cornu ammonis (CA1) and CA3 subregions, subicular complex (Sub), molecular layer (ML), entorhinal cortex (EC), and layer 1 (L_1). Subregions demarked by red rectangles are shown at higher magnification in B1–B3. Scale bar 200 µm. (*B1–B3*) Higher magnification fluorescence images at the border between the OML of the dentate gyrus and SLM (dashed line) near the pole region (*B1*), the OML/ML border (*B2*), and the OML/IML of the dentate gyrus (*B3*; see areas within the red rectangles in *A*). Note the differences in the density and distribution of CR cells within the selected areas some of which are marked by white arrowheads. For abbreviations see Figure 1A. Scale bar 100 µm. (*C*) Series of multichannel fluorescence images of a CR cell (white arrowhead) and a GABAergic interneuron (asterisk) as shown by DAPI counterstaining. In the next panel the CR cell is labeled by EGFP (arrowhead) but not the GABAergic interneuron (asterisk). Although both neurons express the extracellular matrix protein *reelin*, GABA immunoreactivity is found only in the interneuron as indicated by the cytosolic signal and the merged image. Scale bar 25 µm.

the HF region persisted in mature animals (P30–P60) at values comparable with those observed in the OML_{ip} and L_1 of much younger animals (P8-P15; Fig. 3*B*). Near the HF, CR cell density was decreased by ~85% from P8 (13.8 ± 1.0 cells per 5000 µm^2) to P60 (2.1 ± 0.2 cells per 5000 µm^2). Interestingly, similar decline kinetics were observed in the OML_{ip} (~80% reduction), whereas L_1 of the subicular complex and EC displayed a time course more similar to that observed in the neocortex (~98% reduction, see Chowdhury et al. 2010; Anstötz et al. 2014). In the OML_{ip}, CR cell density decreased from 2.6 ± 0.2 cells per 5000 µm^2 to 0.5 ± 0.1 cells per 5000 µm^2 at P8 and P60, respectively. In L_1, their density was reduced from 4.6 ± 0.5 cells per 5000 µm^2 at P8 to 0.1 ± 0.0 cells per 5000 µm^2 at P60.

In conclusion, the HF region appears to be an area where CR cells remain an integral part of its mature circuits (Fig. 3*B*). It is important to note that the numerical decrease of CR cell density cannot be fully accounted by the growth of the developing structures and by the resulting cellular dilution (Fig. 3*C*).

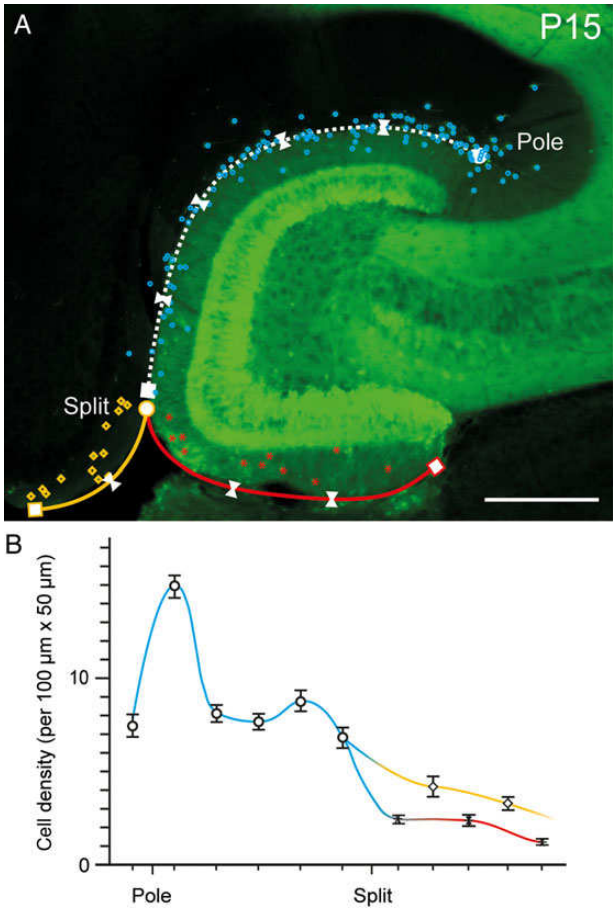

Figure 2. Density and distribution pattern of CR cells in the hippocampus. (*A*) Distribution of EGFP-labeled CR cells in a horizontal slice through the hippocampal formation at P15. CR cells are highlighted by different colors indicating their areas of location (blue dots: HF region, red asterisks: OML_{ip} of the dentate gyrus, yellow rectangles: L_1 of the subicular complex/entorhinal cortex). Split indicates the pial fusion point. White triangles mark the different counting areas along the HF. Pole indicates the termination of the hippocampal fissure in the CA3 subregion. Scale bar 250 µm. (*B*) Summary line histogram of the density of CR cells along the various regions of the hippocampal formation color coded as in *A*. Note the steep increase and plateau in the number of CR cells along the HF (blue line) and the steady decline in L_1 (yellow line) and OML_{ip} (red line).

In the neocortex, the disappearance of CR cells has been suggested to be driven by caspase 3-dependent apoptotic processes (Chowdhury et al. 2010; Anstötz et al. 2014). In the hippocampus, CR cells displaying signs of degeneration were also observed as early as P15 (Fig. 3*D1*-*D2*). Interestingly, however, degenerating cells were almost immunonegative for reelin (Fig. 3*D1*) and, surprisingly, they did not appear to express cleaved-caspase 3 (Fig. 3*D2*).

Structural Properties of CR Cells: Somatodendritic Configuration, Axonal Arborization, and Density of Synaptic Varicosities

In order to analyze the structural properties and synaptic connectivity of CR cells, 121 EGFP-positive neurons both in the SLM and in the OML (Fig. 4*A*–*E*, range: P6-P21) were intracellularly filled with biocytin. From that sample, 68 CR cells met our criteria for post hoc LM analysis, quantitative reconstructions and subsequent EM. The somata of the recovered neurons had ovoid to elongated shape (Fig. 4*A*–*E*) with a mean horizontal diameter of 12.6 ± 2.3 µm (see Table 1), some of which bore somatic spines (Fig. 4*B1*). CR cells were typically characterized by a prominent horizontally oriented thick stem dendrite originating from one pole of the soma (Fig. 4*A*–*E*). The majority of stem dendrites had a significant trend being oriented toward the HF, independently of their origin in SLM or the OML (Figs 4*A*, *B1*, *B2*, *C*,*D*, 6*A*). Some could be followed over long distances (Fig. 4*C*); with a mean total dendritic length of 226.9 ± 133.3 µm (minimum: 10.0 µm; maximum: 550.6 µm; see also Table 1). In most cases the stem dendrite gave rise to several secondary and tertiary side branches of various length (Fig. 4*B2*, *C*,*E*) mainly running parallel to the stem dendrite (Fig. 4*C*). Occasionally, CR cells formed a complex, sometimes vertically oriented, terminal tuft at the most distal portion of the stem dendrite (Fig. 4*B2*, *C*,*E*). The majority (95%, 63/68 cells) of CR cell dendrites were densely covered with spine-like, filopodial protrusions (Fig. 4*B*–*E*, inset in *E*). However, rare neurons with a smooth stem dendrite without any appendages and only short side branches were also found (5%, not shown). The dendritic domain of CR cells was mainly confined to the layer of origin of their somata (Fig. 5*A*, white dots in 5*B1*–*B2*) with only a small fraction (7.3%) of dendrites crossing the hippocampal fissure to either invade the OML (Figs 4*C*, 5*A*, 5*B1*) or SLM (Figs 4*D*, 5*A*, 5*B2*). However, the distribution profile of the dendritic domains of all biocytin-filled neurons covering a relatively large area of the SLM or OML (Fig. 5*B3*) suggested that CR cells receive dense, layer-specific synaptic input. In addition, some dendritic branches terminated in large varicosities with a growth-cone like structure (Fig. 4*F*).

The main axons of CR cells (Figs 5*A*, 5*C1*–*C3*, 6*B*, 7*A*,*B*) nearly always emerged from the opposite pole of the soma (Figs 4*B*–*E*, 6*B*), and formed a relatively dense network in either the SLM or OML (Fig. 5*A*, *C1*-*C3*). In addition, we observed CR cells with individual long-range axonal collaterals projecting along the hippocampal fissure (Figs 5*A*, 7*A*, 8*C1*) into various subregions of the hippocampal formation (Figs 5*A*, 8*C1*-*C3*). Along its course, the main axon gave rise to several collaterals (Fig. 7*A*,*B*) of different length and orientation (Figs 5*A*, 6*B*). Occasionally, these collaterals would trespass (Figs 5*A*, 7*C*) and terminate outside their layer of origin (Figs 5*A*, 8*C1*).

CR cells possessed a relatively high density of varicosities per axonal length (Fig. 7*D*,*E*). On average, we measured 24.1 varicosities per 100 µm axonal length. Interestingly, no significant differences were found in the distance between consecutive varicosities in proximal versus distal portions of the axon (Fig. 7*E*). The resulting uniform high density of varicosities along the axon may reflect a high degree of functional connectivity with postsynaptic target cells such as GABAergic interneurons (Quattrocolo and Maccaferri 2014) and, possibly, pyramidal and granule cells.

Next, we tested the hypothesis that varicosities were indeed synaptic boutons by performing immunolabeling experiments for the presence of vesicular glutamate transporters. In all axonal segments examined, varicosities were immunopositive for vGluT2 (Fig. 7*F1*, *F2*), but immunonegative for vGluT1 or vGAT. This result is consistent with previous work on CR cells of the embryonic brain (Ina et al. 2007), and supports the interpretation that axonal varicosities are indeed glutamatergic presynaptic terminals (Quattrocolo and Maccaferri 2014). In contrast, growth cone-like structures observed at the end of some axonal collaterals were immunonegative for vGluT2 (Fig. 7*G1*–*G2*) and all other vesicular transporters tested (vGluT1, vGAT, not shown).

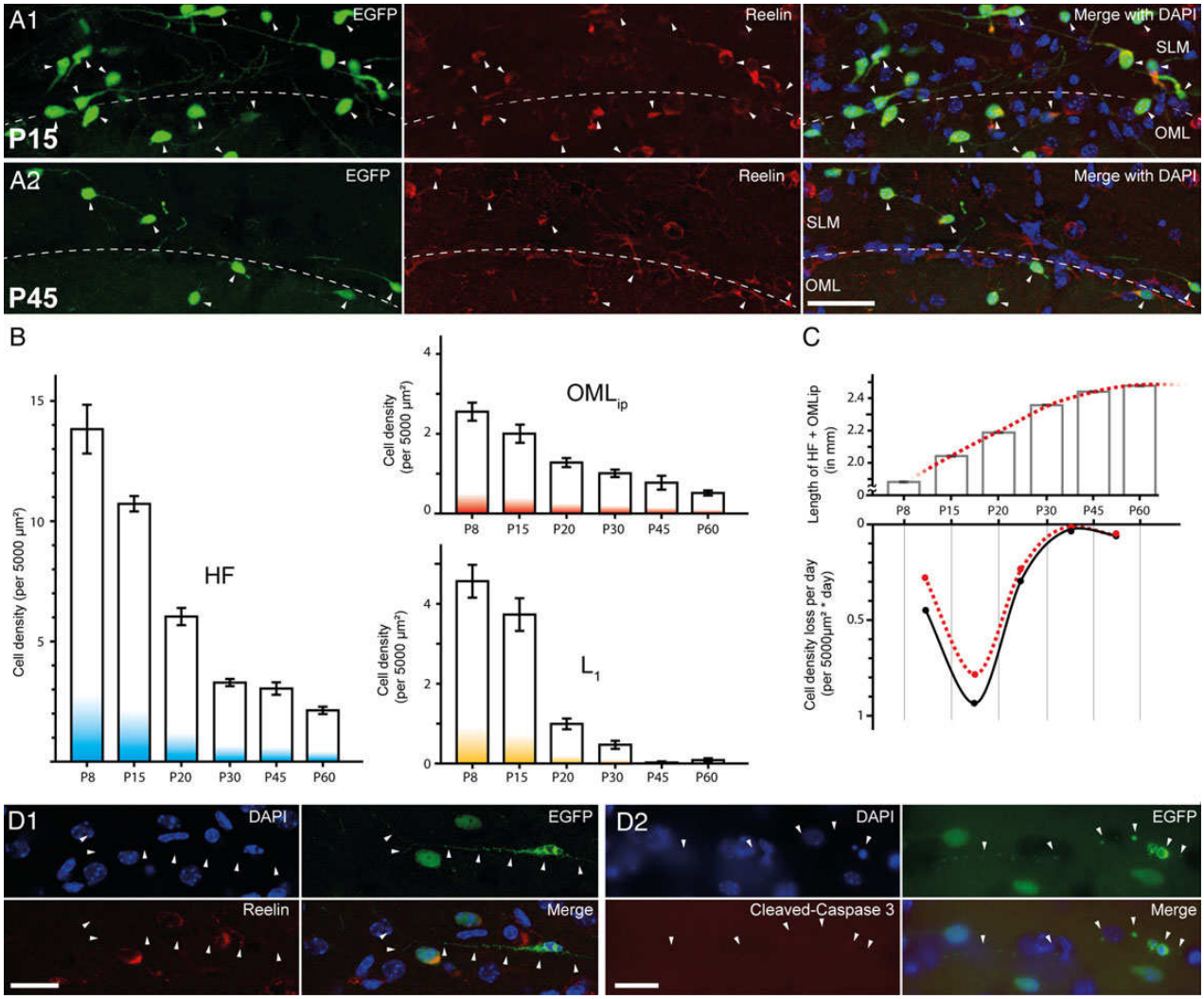

Figure 3. Developmental-dependent decline of CR cells in the hippocampal formation. (*A1,A2*) Multichannel fluorescent images showing the distribution of EGFP-labeled CR cells at the HF (dashed line; left panel), which are all reelin-positive (middle panel) and the merge image (right panel, with added DAPI counterstain) at P15 (*A1*) and at P45 (*A2*). Scale bar 50 µm. (*B*) Bar histograms showing the time course of CR cell density decline along the HF region (left panel), at the OML_{ip} of the dentate gyrus (upper right panel), and L_1 (lower right panel). Note the different time course of CR cell loss in the 3 subregions. (*C*) Upper panel: summary graph of the developmental growth of the HF-OML_{ip} border length between P8 and P60. Lower panel: average density loss of CR cells per day during the same developmental time points shown in *B* before (black dots and curve) and after correction for hippocampal growth (red dots and dashed curve). (*D1*) Multichannel fluorescent images demonstrating early state apoptosis of an EGFP-labeled CR cell with the typical signs of degeneration (pyknotic nucleus and condensed cytoplasm). Notice the lack of reelin immunoreactivity. (*D2*) Another example of an apoptotic EGFP-labeled CR cells. Note the lack of cleaved caspase 3 immunoreactivity in the CR cell. Scale bar *D1–D2* 25 µm.

Analysis of CR Cell Structure Reveals 3 Putative Neuronal Populations

The projection pattern and targeting of biocytin-filled CR cells (P6–P21) allowed us to classify recovered neurons in 3 main subclasses (Figs 5, 8).

The first population, which we termed "local nonprojecting CR cells" ($n = 24$), included neurons with axons confined within their layer of origin. This type was found both in the OML and in SLM, often running parallel towards the HF. Axonal collaterals often covered nearly the entire extension of the OML or SLM (Figs 5A, C1–C3, 8A1, A2) and termination sites could be identified within the prospective layer (Fig. 8A1 inset). Overall, axons had a mean maximum field span of 548.3 ± 238.8 µm (minimum: 156.0 µm; maximum: 999.8 µm; see also Table 1) and an average total length of 1552.3 ± 875.0 µm.

The second group, "local-projecting CR cells" ($n = 22$), was comprised of neurons with an axonal arborization mainly confined to the layer of origin either within the SLM or OML. However, individual collaterals crossed the HF and projected into the adjacent stratum (Figs 5A, 8B1, B2). After crossing, these collaterals would either terminate or turn back into their layer of origin, sometimes with a dense axonal field around the somata. These axons had a mean maximum field span of 450.4 ± 187.9 µm (minimum: 128.1 µm; maximum: 831.0 µm; see also Table 1) and an average total length of 1722.8 ± 1165.7 µm.

The third subtype ($n = 22$) contained neurons with long-range axonal collaterals, which projected beyond the adjacent layer, often to distant target regions of the hippocampal formation (Figs 5A, 8C1, 8C2). Therefore, these cells were referred to as "long-range projection CR cells." Collaterals originating from

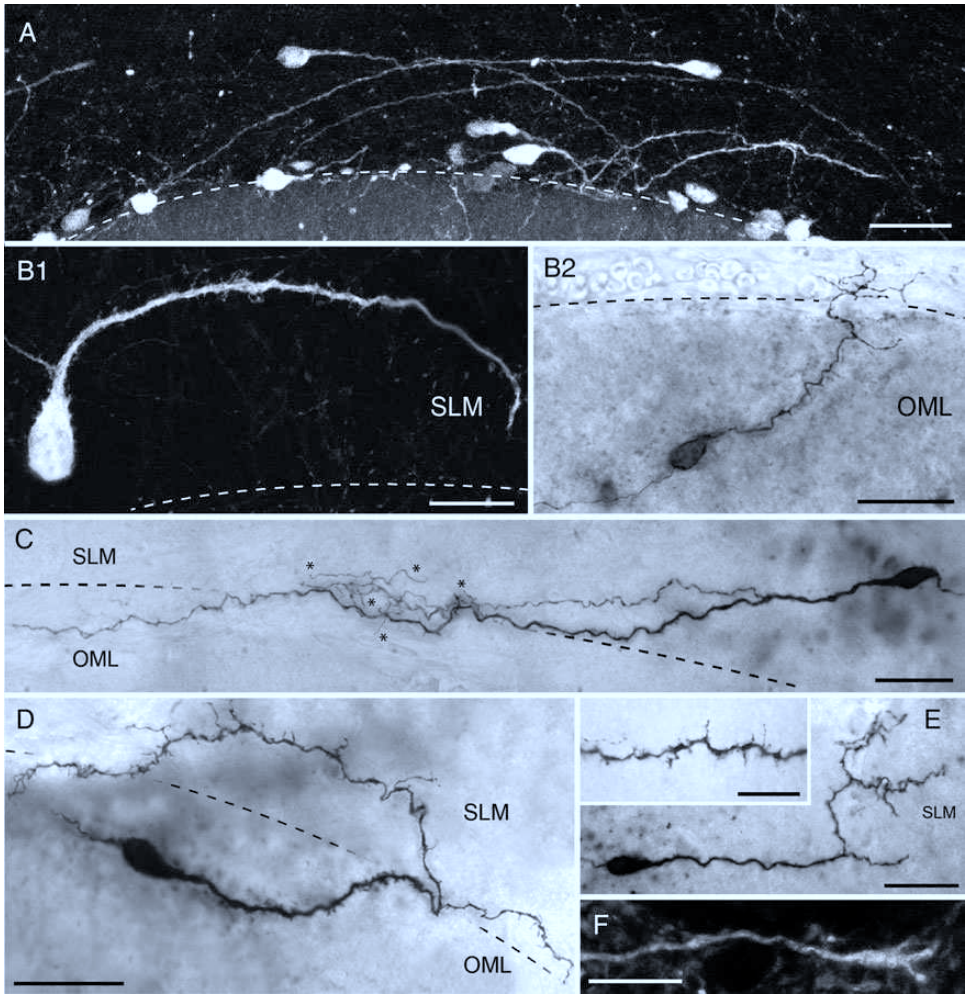

Figure 4. Dendritic morphology of hippocampal CR cells. (*A*) Fluorescence micrograph showing the density and distribution pattern of EGFP-CR cells close to the HF as indicated by the dashed line. Note that the stem dendrites of CR cells are mainly oriented toward the hippocampal fissure regardless of the somatic orientation. Scale bar 50 µm. (*B–E*) Heterogeneity of the dendritic arborization of CR cells, despite the characteristic bipolar morphology with the stem dendrite emerging from one pole of the soma and the axons from the opposite pole. Note the differences in length and complexity of the dendritic trees of sample cells and the variable density in spine- and/or filopodial-like appendages (compare *B*,*D* and *E* with *B2* and *C*) on the dendritic arborization. Notice also the presence of somatic spine-like structures (*B1*). (*F*) High magnification of a dendrite with a growth-cone like structure at its tip. Scale bar in *B–E* 25 µm, in *F* 2 µm and 10 µm in the inset in *E*.

these neurons were seen to project and terminate in the subiculum (Sub), presubiculum (PreSub), parasubiculum (ParaSub) and occasionally in L_1 of the EC (Figs. 5A, 7C, 8C1, C2). These axons had a mean maximum field span of 777.2 ± 311.8 µm (minimum: 272.9 µm; maximum: 1486.5 µm; see also Table 1) and an average total length of 2445.0 ± 1305.8 µm.

Interestingly, no significant differences in the distribution of these cell types were found between CR cell with their somatic origin in SLM and OML. Furthermore, no shift in the proportion of the specific CR cell subtypes was observed at different developmental stages.

Intrinsic Electrophysiological Properties and Firing Patterns

Despite the previously described categorical subdivisions based on the projection of the axon, the membrane properties and firing patterns of all CR cells appeared similar (insets of Fig. 8A1–C1). We could not find any obvious heterogeneity in CR cells with axons of very different lengths. As shown in Figure 9A–D, the injection of hyperpolarizing current pulses revealed large voltage responses, often with a typical sag, consistent both with the high membrane input resistance of these neurons (Marchionni et al. 2010) and with their expression of the hyperpolarization-activated current (Kilb and Luhmann 2000). In addition, low amplitude depolarizing current pulses were able to trigger trains of action potentials of decreasing amplitudes eventually reaching depolarization block, as previously described both in the hippocampus (Marchionni et al. 2010, 2012; Quattrocolo and Maccaferri 2013, 2014) and in the neocortex of this mouse line (Anstötz et al. 2014).

Postsynaptic Target Structures of Hippocampal CR Cells in CXCR4-EGFP Mice

As already mentioned, CR cells in the SLM and OML showed a high density of synaptic varicosities expressing VGluT2 along their axon collaterals (Fig. 7D–F). This suggested that these varicosities are indeed presynaptic boutons. To further corroborate this interpretation, their structure was examined at the EM level ($n = 8$ cells; Fig. 10). OLM and SLM varicosities were easily identified by the dark DAB-reaction product in biocytin-filled

Table 1 Structural and functional parameters of hippocampal CR cells investigated

Name	Layer of origin	Projection type	Soma diameter (µm)	Total length dendrites (µm)	Dendritic endings	Total length axons (µm)	Axonal field span (µm)	Axon endings	Post natal age	R_m (GΩ)	Holding current at −60 mV (pA)
40_23910E	OML_{sp}	Nonproj.	16.1	367.90	3	329.0	276.50	2	14	4.3	−8.79
10_101012A	OML_{sp}	Nonproj.	12.0	188.30	5	494.6	343.50	2	15	1.7	−22.90
45_DEC-16-2010A	OML_{ip}	Nonproj.	13.9	297.80	3	574.5	181.30	5	11	1.4	−26.37
2_DEC162010E	OML_{sp}	Nonproj.	11.4	302.50	8	1178.0	337.40	7	11	1.2	−14.71
53_10_DEC_3A	OML_{sp}	Nonproj.	13.7	294.00	1	1331.1	529.20	3	15	1.2	−34.11
8_101014D	OML_{sp}	Nonproj.	14.1	355.10	4	1368.0	576.10	5	17	4	−13.86
51_101102C	OML_{sp}	Nonproj.	12.0	244.10	3	1386.2	471.60	7	15	2.2	−9.01
72_DEC172010A	OML_{sp}	Nonproj.	13.8	302.40	10	2206.9	971.90	12	12	2.2	−14.93
48_10DEC01E	OML_{ip}	Nonproj.	12.9	191.60	3	2212.4	619.20	18	13	1.2	−32.10
56_101013E	OML_{sp}	Nonproj.	12.5	33.70	1	2344.8	655.00	10	16	1.6	−18.05
43_10_DEC_3C	OML_{ip}	Nonproj.	12.3	340.70	3	2928.2	855.30	9	15	3	−11.52
71_DEC172010H	OML_{sp}	Nonproj.	10.2	174.70	8	3208.5	999.80	15	12	2.3	−17.40
2_DEC162010F	OML_{sp}	Nonproj.	12.4	88.00	1	3562.4	933.50	15	11	2.9	−13.98
33_21910B	SLM	Nonproj.	13.7	223.70	8	177.7	156.00	1	12	1.7	−24.32
67_101014A	SLM	Nonproj.	15.3	113.30	4	708.7	269.10	5	17	1.7	−16.48
37_101021D	SLM	Nonproj.	16.2	90.00	1	710.3	518.60	2	16	2.7	−15.10
35_20910G	SLM	Nonproj.	9.5	305.80	6	862.2	375.90	4	11	1.4	−22.61
44_DEC092010C	SLM	Nonproj.	12.8	74.90	1	1067.9	299.70	6	14	2.2	−17.71
5_101015D	SLM	Nonproj.	11.8	388.10	5	1085.2	355.90	4	18	1.6	−29.50
64_101007F	SLM	Nonproj.	14.9	323.30	15	1495.3	731.90	13	14	1.6	−28.28
66_101013E	SLM	Nonproj.	9.2	405.90	6	1839.0	785.70	10	16	1.5	−18.05
14_101008G	SLM	Nonproj.	17.0	161.70	5	1901.5	576.40	7	15	2.1	−14.60
62_20910A	SLM	Nonproj.	12.5	550.60	10	2085.4	664.90	4	11	1.8	−18.67
54_DEC-16-2010C	SLM	Nonproj.	17.7	298.40	8	2198.3	674.50	9	11	1.3	−28.63
26_10927H	OML_{sp}	Local proj.	13.0	161.40	1	401.3	225.30	4	20	1.3	−8.58
9_101012E	OML_{sp}	Local proj.	11.2	264.90	1	571.2	413.40	3	15	2.3	−23.05
6_101022B	OML_{sp}	Local proj.	14.3	230.40	8	728.6	272.60	3	17	2	−10.81
65_100810A	OML_{sp}	Local proj.	13.8	67.40	1	825.7	340.00	3	15	2	−19.61
6_101022A	OML_{sp}	Local proj.	15.5	57.20	2	923.6	402.10	3	17	1.7	−23.17
45_DEC-16-2010B	OML_{sp}	Local proj.	13.2	55.70	1	975.4	321.20	4	11	1.5	−38.91
16_101007A	OML_{sp}	Local proj.	13.8	227.90	6	983.4	223.50	4	14	2.1	−14.07
33_21910A	OML_{sp}	Local proj.	11.1	319.40	2	1203.0	245.30	5	12	2.9	−12.70
61_101015E	OML_{sp}	Local proj.	13.6	17.30	1	1395.1	589.50	5	18	1.8	−29.04
69_10929B	OML_{sp}	Local proj.	17.5	29.60	1	1818.6	474.70	7	14	1.5	−15.38
59_101021A	OML_{sp}	Local proj.	12.2	74.60	1	1927.2	496.20	9	16	1.6	−26.05
1_DEC162010G	OML_{sp}	Local proj.	15.6	88.20	2	2132.4	451.20	9	11	2.6	−10.43
69_10929A	OML_{sp}	Local proj.	16.2	156.30	8	2395.5	719.70	9	14	1.7	−10.09
60_DEC172010C	OML_{sp}	Local proj.	15.0	73.80	1	3255.1	629.90	11	12	1.7	−18.22
73_DEC152010A	OML_{sp}	Local proj.	19.0	270.90	14	3612.9	532.50	25	18	1.3	−26.13
49_101103A	OML_{sp}	Local proj.	10.4	178.80	2	3914.4	831.00	11	16	1.5	−25.06
7_101013A	SLM	Local proj.	10.2	534.20	19	468.9	128.10	4	16	2.3	−6.03
23_10929E	SLM	Local proj.	14.1	285.50	9	533.1	253.50	3	14	2.5	−14.69
26_10927G	SLM	Local proj.	12.6	40.40	1	866.1	390.20	6	20	2.3	−5.43
75_20930G	SLM	Local proj.	9.2	295.60	9	1456.7	479.00	4	15	2.2	−21.99
74_10DEC1D	SLM	Local proj.	11.7	315.10	11	3122.7	695.00	13	13	1.6	−20.58
63_20910C	SLM	Local proj.	14.4	408.50	9	4391.2	794.50	24	11	1.4	−23.21
57_101020C	OML_{sp}	Long-range proj.	11.8	413.70	18	1237.8	465.10	4	15	2.2	−27.08
46_101014E	OML_{sp}	Long-range proj.	11.6	265.60	4	1399.5	333.10	10	17	1.6	−11.85
52_101020A	OML_{sp}	Long-range proj.	10.9	82.70	1	1446.8	427.80	8	15	1.8	−18.58
47_10_DEC_1A	OML_{ip}	Long-range proj.	14.1	351.30	1	1476.6	272.90	3	13	1.2	−53.49
12_101011E	OML_{sp}	Long-range proj.	17.8	165.60	5	1551.0	633.70	7	14	1.3	−16.86
25_10929G	OML_{sp}	Long-range proj.	12.3	135.30	1	1993.3	683.50	8	14	3.2	−7.24
75_20930F	OML_{sp}	Long-range proj.	11.7	277.40	4	2164.6	745.80	6	15	1.7	−18.26
71_DEC172010G	OML_{sp}	Long-range proj.	10.9	90.60	2	2488.7	952.60	8	12	1.4	−19.57
5_101015C	OML_{sp}	Long-range proj.	12.1	361.80	8	3115.8	918.40	6	18	1.9	−21.46
60_DEC172010D	OML_{sp}	Long-range proj.	14.9	409.60	2	3134.0	1486.50	15	12	2.1	−0.35

Continued

Table 1 Continued

Name	Layer of origin	Projection type	Soma diameter (µm)	Total length dendrites (µm)	Dendritic endings	Total length axons (µm)	Axonal field span (µm)	Axon endings	Post natal age	R_m (GΩ)	Holding current at −60 mV (pA)
64_101007E	OML_{sp}	Long-range proj.	12.4	202.90	4	3590.6	862.40	13	14	1.7	−18.30
3_101021F	OML_{sp}	Long-range proj.	11.0	162.50	5	3603.2	1050.00	22	16	2	−17.73
70_DEC-09-2010E	OML_{ip}	Long-range proj.	10.6	166.90	1	3843.8	1138.70	15	14	1.4	−26.81
54_DEC-16-2010D	OML_{sp}	Long-range proj.	13.5	60.40	22	4218.8	933.60	9	11	2.6	−11.34
36_15910C	OML_{sp}	Long-range proj.	15.6	72.00	2	6675.2	1327.30	29	6	1.3	−23.58
42_DEC082010E	SLM	Long-range proj.	8.5	450.10	2	927.7	496.80	5	15	2.7	−16.38
11_101012D	SLM	Long-range proj.	14.6	497.80	20	1238.1	498.00	4	15	3.5	−7.63
52_101020B	SLM	Long-range proj.	10.6	266.00	7	1312.9	651.00	4	15	2.7	−18.18
31_23910C	SLM	Long-range proj.	13.3	200.70	3	1348.3	462.50	4	14	1.9	−10.09
68_101021E	SLM	Long-range proj.	8.8	316.00	4	1924.6	680.60	9	16	3.1	−7.59
58_101020E	SLM	Long-range proj.	9.4	202.10	2	2030.8	929.10	9	15	3.6	−13.28
57_101020D	SLM	Long-range proj.	10.1	10.00	1	3068.6	1147.90	10	15	2.6	−6.60
Mean			12.97	226.92	5.16	1896.31	590.66	8.1	14.3	2.03	−18.34
SD			2.3	133.26	5.0	1211.1	289.9	5.7	2.4	0.7	8.7
Max			19.0	550.60	22.0	6675.2	1486.5	29.0	20.0	4.3	−0.4
Min			8.5	10.00	1.0	177.7	128.1	1.0	6.0	1.2	−53.5

Note: Quantitative and qualitative parameters based on NEUROLUCIDA reconstructions and electrophysiological examination of hippocampal CR cells ($n = 68$). The projection type was determined by the individual axonal arborization. All numerical values are summarized by mean-, SD-, maximum- and minimum- values. SLM, stratum lacunosum-moleculare, OML_{sp} and OML_{ip}, supra- and infrapyramidal blade of the outer molecular layer of the dentate gyrus, respectively.

(Fig. 10A; $n = 43$) and EGFP-DAB-labeled varicosities (Fig. 10A2, B1, B2; $n = 63$). In the majority of cases they were characterized by the presence of vesicles of various size, and formed connections with a clearly identifiable synaptic cleft and postsynaptic density (Fig. 10A2,B1,B2). In 91.8% of the varicosities in the OML and 93.2% in SLM an active zone (the structural equivalent for a functional transmitter release site) with the postsynaptic target structure was established (Fig. 10C1,C2) which further supports the functionality of these varicosities. In both layers, the majority of synaptic contacts originated from en passant axons and were established on dendritic shafts (~85%, $n = 100$) of variable size (Fig. 10A1,A2,B2). Alternatively, they were found on spines (Fig. 10B1). This result suggests that CR cells target dentate gyrus granule cells in the OLM in addition to GABAergic interneurons and pyramidal cells in SLM (Quattrocolo and Maccaferri 2014).

Paired Recordings Reveal Unitary EPSPs Generated by CR Cells on Interneurons

Using optogenetic stimulation, Quattrocolo and Maccaferri (2014) recorded the synaptic output of channelrhodopsin-expressing CR cells onto both hippocampal GABAergic interneurons and pyramidal cells. However, this technique suffers from the limitation that optogenetically evoked responses are the result of the activation of an unknown number of presynaptic CR cells. Therefore, the impact of a unitary connection on the membrane potential of the postsynaptic neuron remains unresolved.

To readdress this issue, we took advantage of paired recordings, which allow the measurement of the postsynaptic effect generated by a single neuron. From a sample of 146 simultaneous recordings from CR cells and SLM, functional synaptic connections were found in 5 cases. In one case, we could fully recover the anatomy of both the presynaptic CR cell and the postsynaptic interneuron (Fig. 11A1–A3, B). Two putative light microscopically identified synaptic contacts were observed on different distal dendritic branches of the GABAergic interneuron (Fig. 11A2-A3). In the remaining 4 experiments only partial anatomical recovery was achieved. Postsynaptic interneurons were located close to the hippocampal fissure ($n = 3$ cells with multipolar dendritic arborization) or within the fissure itself (one cell: only the soma and the beginning of multiple dendritic trunks were recovered). The axonal branches of the 3 partially recovered interneurons were either restricted to SLM ($n = 1$) or could be found both in SLM and OML ($n = 2$).

Functionally, action potentials triggered by brief current injection in the presynaptic CR cells generated uEPSPs in GABAergic interneurons (Fig. 11C1–C2). Analysis of the averaged uEPSPs for these 5 connections (Fig. 11C2) revealed a peak amplitude of 3.2 ± 1.0 mV, a 20–80% rise time of 3.2 ± 1.2 ms and a 100–37% decay time of 28.4 ± 4.9 ms. Additionally, both the presence of failures (on average ~20% in 4 connections; in the smallest uEPSP they could not be easily identified and therefore were not quantified) and of very large individual responses (reaching several millivolts, see Fig. 11C1) were observed. Application of the AMPA receptor antagonist 2,3-Dihydroxy-6-nitro-7-sulfamoyl-benzo[*f*] chinoxalin-2,3-dion (NBQX, 20 µM) completely abolished the postsynaptic effect, thus indicating that uEPSPs at resting membrane potentials were mediated by AMPA-type glutamate receptors ($n = 3$ pairs). This result confirms indisputably the excitatory nature of CR cells and fits well with the evidence that CR cells powerfully drive feed-forward GABAergic input to hippocampal pyramidal neurons (Quattrocolo and Maccaferri 2014). The large amplitude of individual events raises the intriguing possibility that this can be accomplished by very few CR cells, potentially even a single one. Examination of the responses to paired-pulse stimulation (Fig. 11D1,D2) revealed the presence of short-term depression in most connected pairs. Current steps of brief

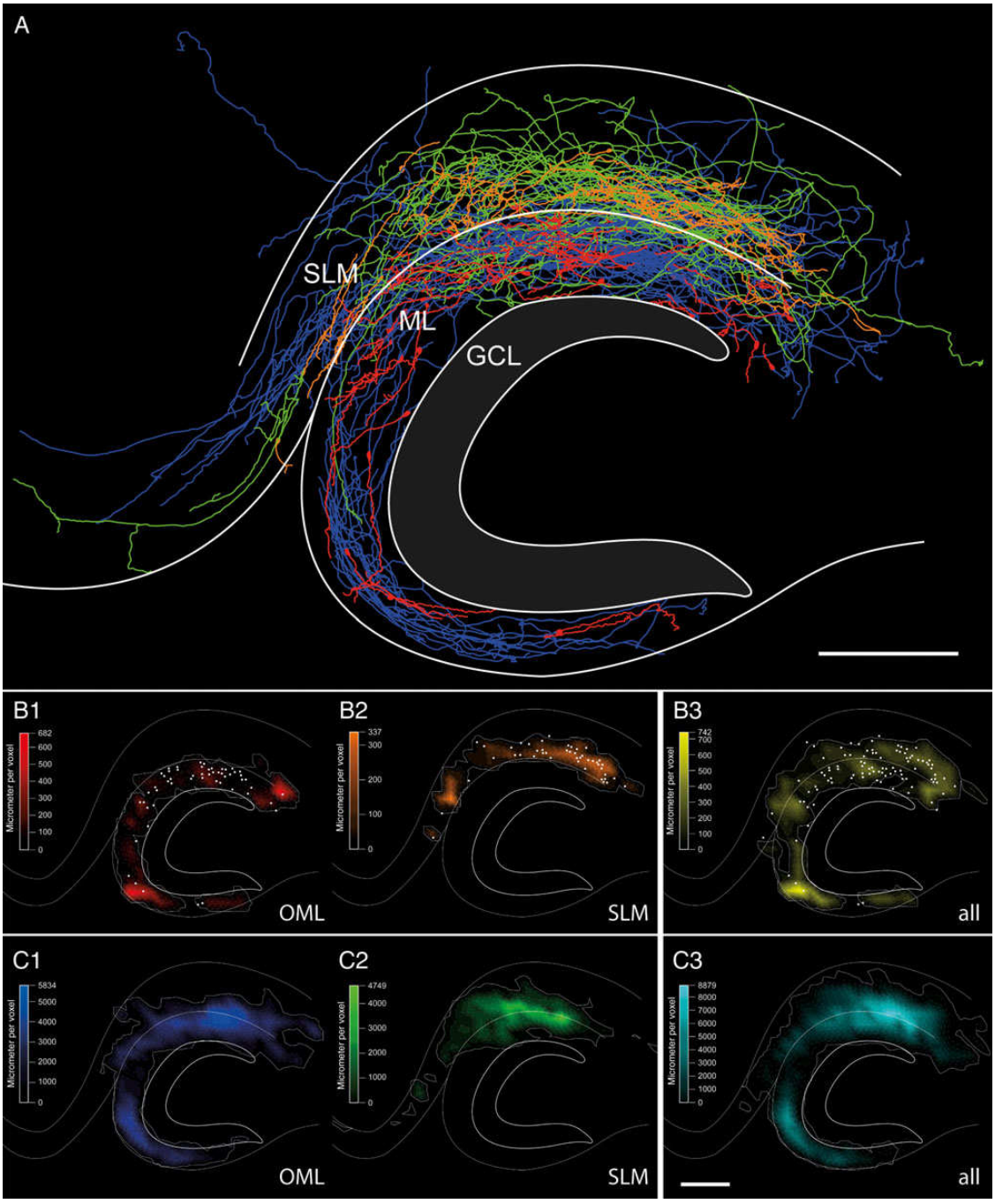

Figure 5. Dendritic and axonal distribution pattern of hippocampal CR cells. (*A*) Summary plot of all reconstructed CR cells merged into a scheme of the hippocampus. The somatodendritic domain of CR cells located in the OML is given in red and that of CR cells in the SLM in orange. The axonal domains are given in blue (OML) and green (SLM), respectively. Note the variability and complexity of the axonal arborization with different projections, covering the entire OML and SLM. Notice also the presence of individual collaterals crossing the hippocampal fissure and projecting to various regions of the hippocampal formation. (*B*,*C*) Quantitative analysis of the dendritic (*B1–B3*) and axonal (*C1–C3*) domains (same color code for OML- and SLM-CR cells as in *A* as shown in a contour plot indicating the density of either the dendritic and axonal segments with respect to their position in the hippocampus. Note that the dendritic domains (*B1*,*B2*) are mainly restricted to the layer of the origin of somata (white dots). OML-CR-cell axons (*C1*) show a relative homogenous density pattern within their layer of origin with projections into the SLM. CR cell axons of the SLM (*C2*) show their highest density near the hippocampal fissure also exceeding the layer border and projecting into distant regions, but not covering the medial part of the OML. Panels *B3* and *C3* show the dendritic (yellow) and axonal (cyan) distribution pattern of all reconstructed CR cells. The white contour around the density distributions indicates the 95% of the total density in the distribution. Voxel size 50^3 µm^3; Scale in *A–C* bar 250 µm.

duration (5 ms) and sufficient amplitude to trigger action potentials were injected in the CR cell at a 100-ms interval to evaluate paired-pulse plasticity. The overall paired-pulse ratio (amplitude of the second uEPSP over the first uEPSP) was 0.77 ± 0.11.

Discussion

In this study, we have described several novel results concerning the structural and functional properties of hippocampal CR cells.

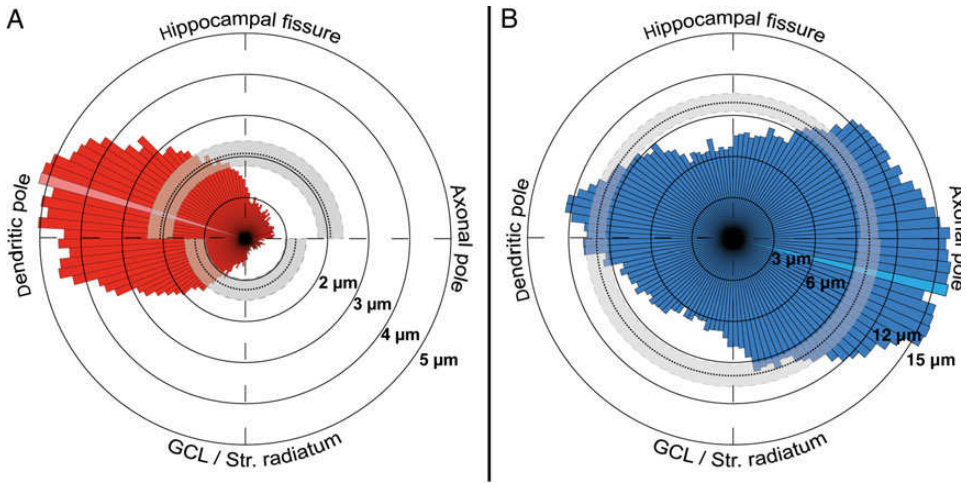

Figure 6. Quantitative analysis of the dendritic and axonal arborization of hippocampal CR cells. (*A*,*B*) Polar plots of the dendritic (red, left panel) and axonal domains (blue, right panel) of all CR cells investigated given as a radial bar histogram with 3° intervals. The dashed lines indicate mean values; gray areas mark the 95% confidence intervals. Maximum values are indicated by the light red and blue region within the histogram, respectively.

First, both their density and developmental regulation in the hippocampal formation are region-specific. Second, although CR cells can be classified into 3 distinct subclasses upon their axonal projection patterns, their basic excitability appears homogenous. Third, CR cell output synapses are biased toward targeting mostly dendritic shafts, and less frequently spines. Last, we have provided unequivocal evidence that hippocampal CR cells are excitatory neurons and may generate large-amplitude uEPSPs in postsynaptic GABAergic interneurons.

Developmental Regulation of CR Cell Densities in the Hippocampal Formation

Our data highlight a profound difference in the postnatal regulation of hippocampal versus neocortical CR cell densities. While neocortical CR cells virtually disappear at around P14, they persist at higher levels in the hippocampus. Work by Chowdhury et al. (2010) in the Ebf2-GFP mouse has described stable density levels of CR cells between P3 and P7, with a dramatic decrease between P7 and P14. Mature final levels (<3.5% of the initial P3-P7 values) were reached after the fourth postnatal week in the neocortex. In contrast, our data show that between P8 and P15, the densities of CR cell of the HF area and OML_{ip} do not decline as dramatically. Furthermore, both regions appeared to preserve ~15–20% P8 density values in mature animals at P60. In contrast, L_1 of the subicular complex/EC showed more similarities to the neocortex, and a near disappearance of CR cells was observed in fully mature mice (~2% of P8 values).

Although we have found that developmentally related structural growth does contribute to the decline of CR cell densities, its role appears minor. In fact, we have found in every region of the hippocampal formation evidence for degenerating CR cells. Surprisingly, this type of degeneration appears to be independent of caspase 3 activation, which, in contrast, has been reported in CR cells of the neocortex (Chowdhury et al. 2010; Anstötz et al. 2014). Therefore, our results suggest that a different type of programmed cell death regulates the disappearance of neocortical versus hippocampal formation CR cells. Intriguingly, caspase-independent programmed cell death has been shown to occur during brain development in caspase-3 and caspase-9 knockout animals, and was reported to affect specific neuronal populations with a delayed onset when compared with wild-type animals (Oppenheim et al. 2001). Although more work is required to define the signals that lead to a specific activation of caspase 3 in the neocortex versus hippocampal formation, the lack of caspase 3-related apoptosis could partly explain the persistence of CR cells in the latter structure.

Layer and Regional Specificity of Hippocampal CR Cells

The long postnatal persistence of CR cells in the hippocampal formation highlights their conventional roles as neurons integrating and relaying information to their prospective synaptic targets. Our results show that CR cells may be subdivided into distinct populations on the basis of the local versus projecting characteristics of their axons. In particular, we have identified CR cells with complete layer-restricted location of both their somatodendritic and axonal domain. This exquisite specificity suggests local functions, i.e., mostly depending on layer-specific input and producing synaptic output affecting the same layer. In general terms, this subclass of hippocampal CR cells, similarly to their counterparts in the neocortex, can be thought as a type of "glutamatergic interneuron" acting either within the HF or OML_{ip} region. In contrast, the observation of CR cells with axons projecting to different layers or even to distant regions of the hippocampal formation suggests the possibility of more complex functions. To our knowledge, our discovery of local-projecting CR cells (whose axons crosses the hippocampal fissure and travel from the SLM to OML or vice versa) is the first evidence of an intrinsic glutamatergic hippocampal connection that does not flow according to the classical direction of the trisynaptic circuit (Andersen et al. 1966). In fact, this type of nonclassical intrahippocampal connectivity has been described only for GABAergic (Sik et al. 1994; Ceranik et al. 1997), but never for glutamatergic connections. It is interesting to note that the synaptic inputs to SLM and OML (Steward and Scoville 1976; but see also Kitamura et al. 2014) originate predominantly from distinct cellular populations in the EC and terminate to different layers in the dentate gyrus and hippocampus proper, which would suggest a high degree of parallel (and separate) processing by the 2 networks. The presence of local-projecting CR cells could provide a cellular substrate for an early integration of these inputs at their entry in the hippocampus.

Last, CR cells with long-range axons (long-range projecting CR cells) that target distant subregions were identified reaching as

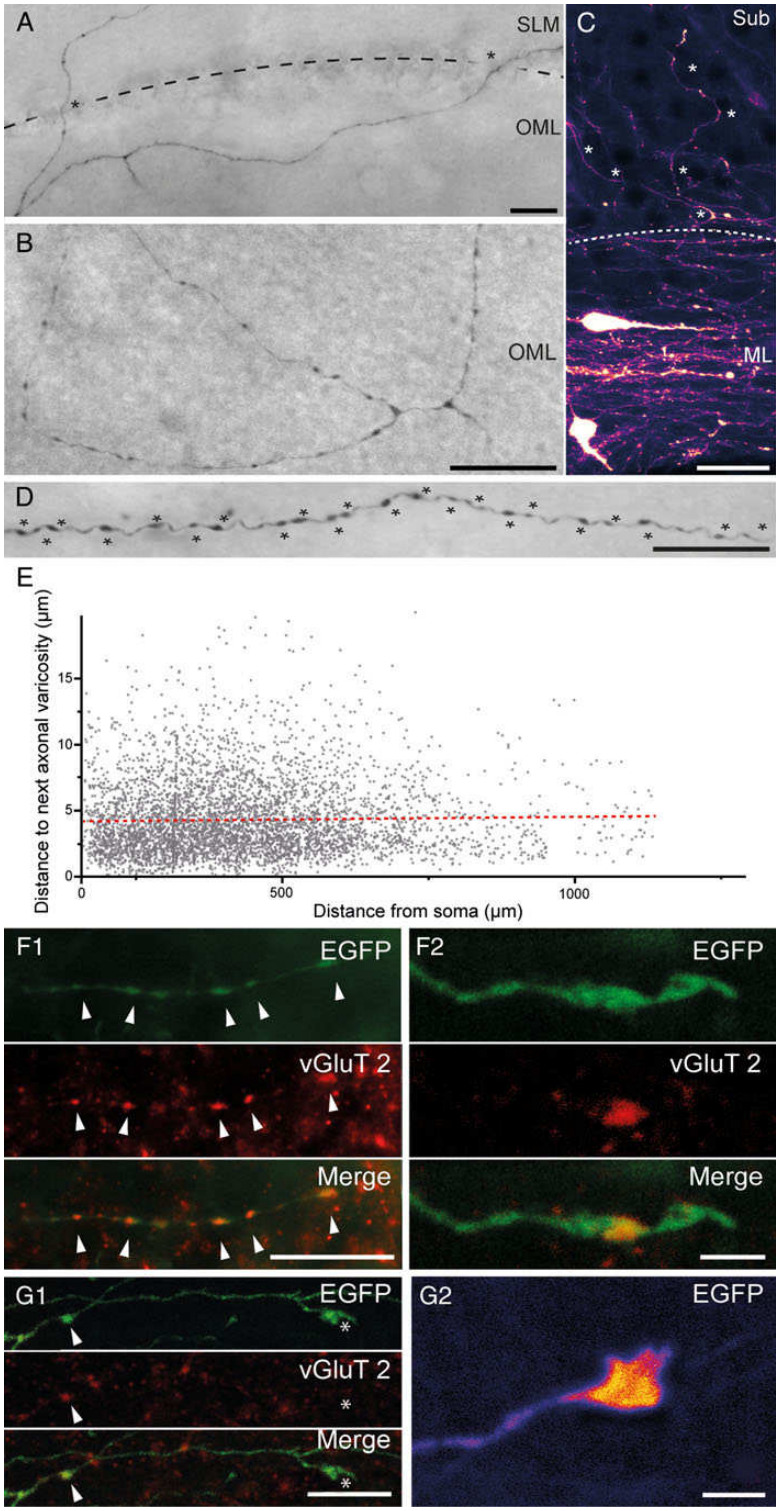

Figure 7. Axonal arborization and synaptic bouton density of hippocampal CR cells. (*A*) Biocytin-filled CR cell with an axon that projects via the HF (indicated by the dashed line). Scale bar 25 µm. (*B*) Axonal branching pattern of another biocytin-filled CR cell with a local, but complex axon confined within the OML of the dentate gyrus. Scale bar 25 µm. (*C*) EGFP-fluorescence image of 2 CR cells within the subicular molecular layer. Note the dense axonal plexus around the neurons with several individual collaterals (marked by asterisks) crossing the molecular layer border (dashed line) to project and terminate in the Sub. Scale bar 20 µm. (*D*) High density of axonal varicosities (marked by asterisks) along an individual axonal collateral of a biocytin-filled CR cell. Scale bar 20 µm. (*E*) Summary plot of the intervaricosity distance along CR cell axons as a function of distance from the soma. Dashed line represents the linear fit ($r^2 = 7.03 \times 10^{-4}$; $f(x) = 3.05 \times 10^{-4}x + 4.15$). (F1) Multichannel fluorescent images of synaptic boutons (marked by arrowheads) of a EGFP-labeled axonal collateral (top panel), vGluT2 immunohistochemistry (middle panel), and the merged image (lower panel). Note that all varicosities are VGluT2 positive. Scale bar 10 µm. (F2) similar to F1 for a different axon, but shown at higher magnification. Scale bar 2 µm. (G1) Series of 3 low power images of an axonal collateral terminating in a growth cone-like structure (marked by an asterisk). Note that synaptic boutons (marked by arrowheads) express vGluT2 immunoreactivity, which is not found in growth cone-like structures. Scale bar 5 µm. (G2) False-color EGFP fluorescence of a different growth cone-like structure shown at higher magnification. Scale bar 2 µm.

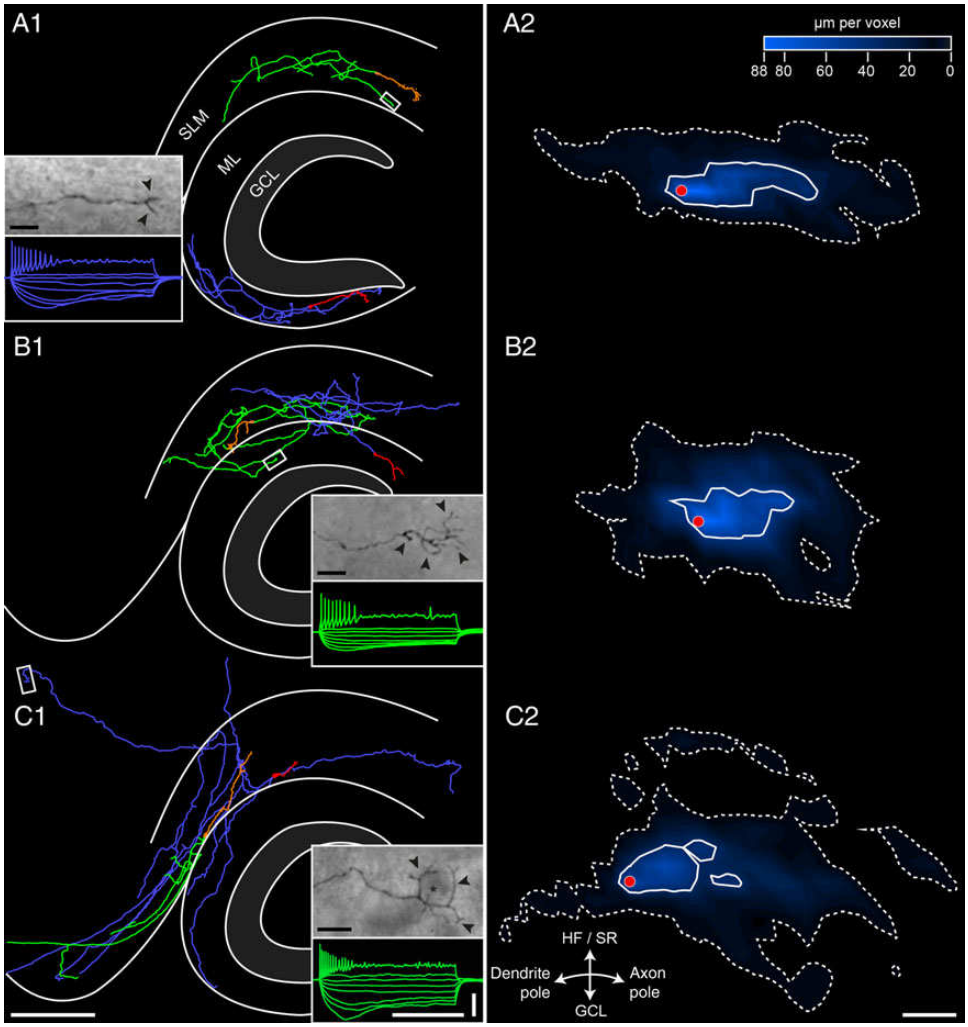

Figure 8. NEUROLUCIDA reconstructions of biocytin-filled hippocampal CR cells. Representative examples of reconstructed hippocampal CR cells filled with biocytin. Their somatodendritic configuration is given either in red or orange, and the axonal domain in blue or green to distinguish between the 2 neurons. The framed area shows the termination of an individual axonal collateral ending in a growth-cone like structures. The characteristic firing patterns of one of the reconstructed neurons is also shown in the corresponding color. (*A1*) Hippocampal CR cells with somata located in the SLM and OML with a local, nonprojecting axonal morphology. One of its axonal collaterals (framed white area) terminates in the SLM. (*B1*) Two CR cells, one with its somatodendritic domain (red) in the OML but with a projection of the majority of axonal collaterals (blue) crossing the hippocampal fissure terminating in the SLM. The other CR cell has its somatodendritic domain in the SLM (orange) but with 2 axonal domains (green), one in the SLM and the other in the OML. One of the green axonal collaterals (framed white area) terminates with a tuft-like structure in the OML. (*C1*) Two CR cells both with a somatodendritic domain located in the SLM with individual long-projecting axons to distant regions of the hippocampal formation with an individual axonal collateral with a basket-like termination (framed white area, inset) in the Sub/EC area. Note the relative small somatodendritic domain (red) of the CR cell with the large axonal arborization (blue) to the EC and OML. Scale bars in A1–C1 are 250 µm for the main figures and 500 ms and 50 mV for all electrophysiological recordings. (*A2–C2*) Summary diagrams of the axonal density and distribution pattern of local, nonprojecting CR cells (*A1*), CR cells with local and projecting collaterals to the SLM or OML (*B1*) and those with long-range projections (*C1*). The white closed contours determine 50% of the maximal axonal density, the dashed contours 5%, respectively. The red dot represents the position of the aligned somata. Note the marked differences in the axonal density and distribution pattern between the 3 populations. Scale bar for A2–C2 250 µm.

far as the Sub, preSub, paraSub, and even the EC. This is consistent with a previous study using retrograde tracing in newborn rats (Ceranik et al. 1999), and expands the significance of this connection to later postnatal stages. It is interesting to note that these long-range target regions host neurons that in vivo may display the firing properties of grid cells (Hafting et al. 2005; Boccara et al. 2010, reviewed by Moser et al. 2008). While the basic properties of place cells of the hippocampal formation seem to be already present in immature animals at their first navigational experience, grid cells develop later and appear roughly at the third postnatal week in rats (Langston et al. 2010; Wills et al. 2010, 2012). We suggest that long-range glutamatergic input from hippocampal CR cells may activate postsynaptic receptors of the AMPA- and NMDA-type onto target neurons in the Sub, preSub, paraSub, and EC, thus contributing, at early developmental stages, to the hippocampal-originated excitatory drive that is required by grid cells (Bonnevie et al. 2013). At present time, however, the cellular targets of long-range projecting CR cells remain unknown and future work is needed to confirm our hypothesis, which remains speculative. If this were the case, however, this circuit could provide a direct functional link between the firing of place cells in the hippocampus proper and distant grid cells. The bursting pattern of hippocampal place cells could easily generate facilitating excitatory postsynaptic

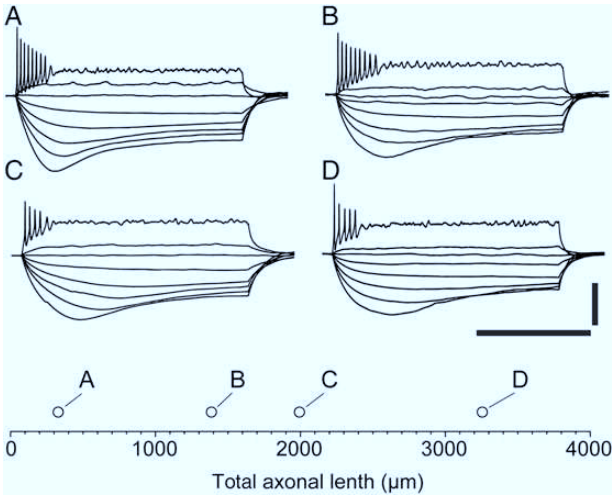

Figure 9. Firing pattern of hippocampal CR cells does not change with axonal length. (*A–D*) The typical firing pattern and membrane responses to various current steps (−50 pA to 10 pA in 5 pA steps and then 55 pA, 1-s duration) is shown for CR cells of various axonal lengths, which is plotted in the bottom inset. Note the similarity of the traces, despite the large difference in axonal length. Scale bar is 500 ms and 50 mV.

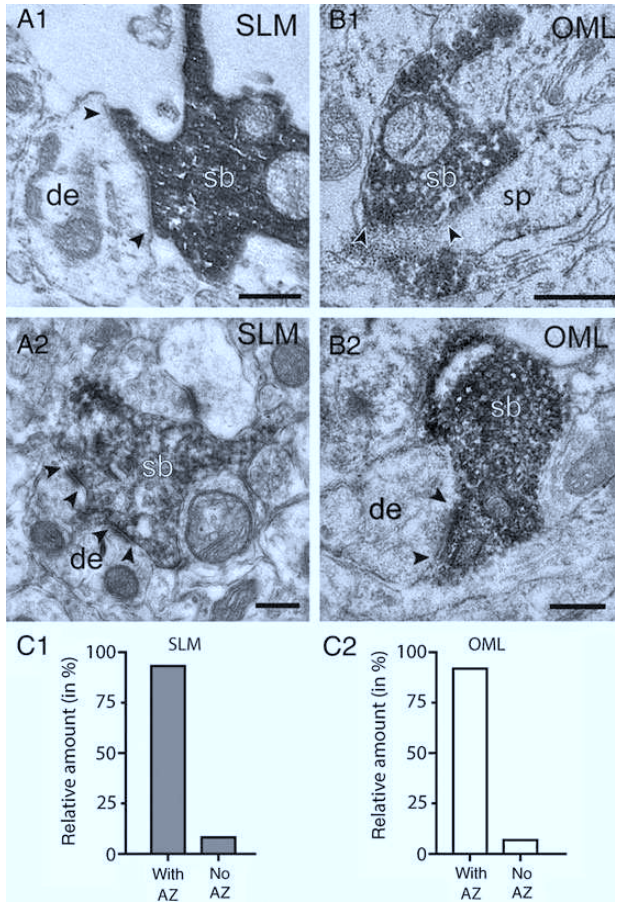

Figure 10. Synaptic output of CR cells onto hippocampal neurons. (*A1,A2*) En passant synaptic boutons (sb) of a biocytin-filled CR cell axonal collateral (dark labeling in *A1*) and an EGFP-converted axon terminal (*A2*, dark DAB-labeled structure) on postsynaptic target dendrites (de) in the SLM. (*B1,B2*) Two representative examples of synaptic boutons (sb) detected by an EGFP-antibody terminating on a spine (sp, *B1*) and a small caliber dendrite (de, *B2*) in the OML. In all panels the active zones at the pre- and postsynaptic apposition zone are marked by arrowheads. Labeled synaptic boutons were identified also by the dense accumulation of synaptic vesicles. Scale bars in A1–B2 0.25 µm. (*C1,C2*) Bar histograms showing the proportion of axonal boutons establishing a synaptic contact with the postsynaptic target structures in the SLM (gray columns) and OML (white columns).

potentials in O-LM GABAergic interneurons and lead them to threshold (Ali and Thomson 1998). O-LM cells, in turn, have been suggested to powerfully excite CR cells (Quattrocolo and Maccaferri 2014). Therefore, we propose that the activation of CR cell projections following bursting in hippocampal place cells (O'Keefe and Dostrovsky 1971; Ranck 1973) might regulate synaptic excitation/plasticity in developing grid cells. This is especially intriguing as hippocampal CR cells are still present in the rodent hippocampal formation at later postnatal stages (Supèr et al. 1998; this study) associated with the abrupt maturation of grid cell properties (Wills et al. 2012). An experimentally testable prediction would be that animals with reduced numbers of CR cells (Meyer et al. 2004; Yoshida et al. 2006; Tissir et al. 2009) would suffer functional alteration or delayed development of grid cell neurons.

Postsynaptic Target Domains of CR Cells

In addition to confirming the presence of CR cell-originated synaptic boutons that do not form synaptic contacts (Marchionni et al. 2010), we provide EM-based structural evidence that the majority of varicosities represent functional transmitter release sites and that hippocampal CR cells contact both dendritic shafts and spines, although the majority were found on dendritic shafts. While synaptic contacts terminating on spines are usually taken as evidence of excitatory synaptic transmission onto pyramidal cells, boutons terminating on shafts are usually interpreted as evidence of transmission onto GABAergic interneurons. Although this interpretation fits very well with physiological data suggesting a connectivity bias favoring interneurons versus pyramidal cells, it needs to be taken into account that excitatory synapses onto pyramidal cell dendritic shafts are extremely rare in SO and SR, but may occur, albeit in limited numbers, in the SLM (Megías et al. 2001). In addition, there is clear evidence from excitatory intralaminar and translaminar synaptic connections in the neocortex that shaft synapses may be excitatory in nature (Markram et al. 1997; Feldmeyer et al. 1999, 2006). In any case, the presence of synapses on spines reinforces the physiological evidence of a monosynaptic glutamatergic input from CR cells to hippocampal pyramidal neurons (Quattrocolo and Maccaferri 2014). The observation of CR cell excitatory boutons close to dendritic shafts could also be the structural correlate of a synaptotrophic effect (Cline and Haas 2008) mediated by CR cells, as glutamate released onto dendrites has been shown to have the ability to trigger the formation of spines (Kwon and Sabatini 2011). Thus, CR cell boutons forming synaptic contacts on dendritic shafts of pyramidal cells might have an "instructing" developmental role and contribute to the structural maturation of their dendritic tree. Such a role was already emphasized for neocortical CR cells axons by positioning and anchoring terminal tufts dendrites of pyramidal cells in layer 1, thus partially contributing to the establishment of the cortical column (Radnikow et al. 2002; Anstötz et al. 2014). This may result in an integrated synaptic activity of developing pyramidal cells by the activation of Ca^{2+} spikes in pyramidal cells across columns, thereby contributing to the establishment of early cortical domains.

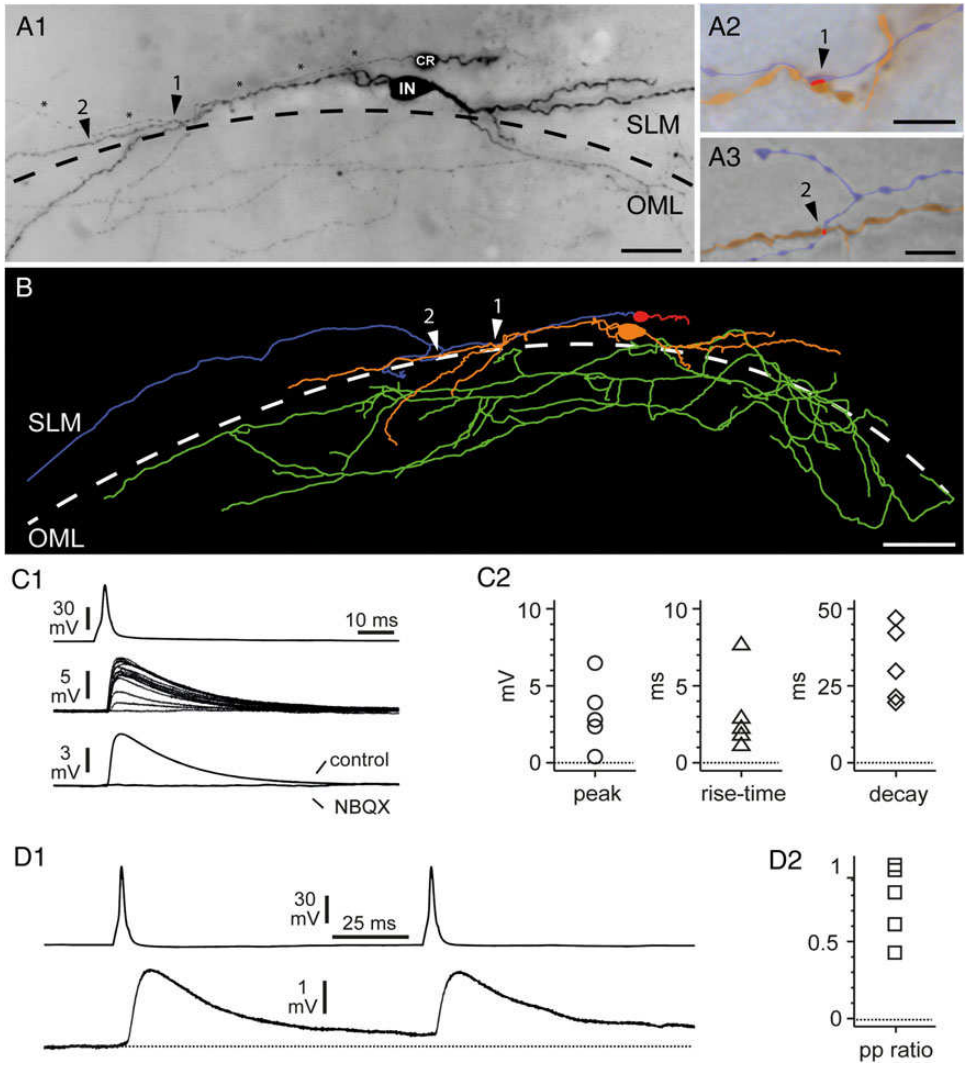

Figure 11. Morphology and basic functional properties of a CR cell to a GABAergic interneuron synaptic connection. (*A1*) Light micrograph of a biocytin-filled, synaptically coupled pair between a presynaptic CR cell and a postsynaptic GABAergic interneuron (IN). Both cells were located in the SLM close to the HF (dashed line). Note the CR cell axon (marked by asterisks) running parallel to an interneuron dendrite establishing 2 putative light microscopically identified synaptic contacts, marked by arrowheads, and numbers. Slice obtained from a P17 mouse. (*A2,A3*) High-power light microscope images of the 2 putative light microscopically identified synaptic contacts of the presynaptic CR cell axon (blue) with the postsynaptic interneuron dendrite (orange) as indicated by arrowheads. The putative contact area is highlighted in red. (*B*) NEUROLUCIDA reconstruction of the synaptically coupled pair shown in A1. The somatodendritic configuration is given in red (CR cell) or orange (IN) and the axonal domain in blue or green, respectively. The putative synaptic contacts are marked by white arrowheads and numbers. Scale bars in A1 25 µm, (*A2–A3*) 5 µm and B 50 µm. (*C1*) Paired recording between a presynaptic CR cell and a postsynaptic interneuron with the somata on the hippocampal fissure. Current injection triggers a spike in the CR cell (top trace), which generates a uEPSP in the interneuron (middle traces). Notice the variability of the response and the presence of a failure. Notice also that individual response may be very large and reach amplitudes of ~10 mV. The bottom traces show the unitary response recorded in regular ACSF (control) and after the addition of NBQX (20 µM). (*C2*) Summary plots showing the basic properties (peak amplitude, 20–80% rise time and 100–37% decay time) of the uEPSPs recorded in 5 connected pairs. (*D1*) Paired-pulse modulation of CR Cell uEPSPs. The upper trace shows 2 action potentials triggered at 10 Hz in the presynaptic CR cell, whereas the lower trace shows the postsynaptic response. Notice the presence of a mild depression. (*D2*) Summary graph of paired-pulse modulation (peak of the second uEPSP over the peak of the first EPSP: pp ratio) for the 5 connections tested. Notice the presence of short-term depression in most uEPSPs.

Control of Interneuronal Activity by CR Cell-dependent Excitatory Input

Here we provide the first direct evidence of an excitatory monosynaptic CR cell–GABAergic interneuron connection based on paired recordings. This is especially important as previous attempts to find such a connection in the neocortex, (Soda et al. 2003), or hippocampus (Marchionni et al. 2010) had been unsuccessful. While unitary connections between GABAergic interneurons to CR cells are experimentally relatively easy to find (Quattrocolo and Maccaferri 2013), the degree of connectivity observed between CR cells to GABAergic interneurons appears much lower (~3.4%). This probably depends on the much denser axonal arborization of interneurons, which makes it more likely that several axonal branches may be in close proximity to the tested postsynaptic CR cell. In contrast, as shown here, the density of the axonal arborization formed by CR cells decreases rapidly with distance. Therefore, despite a high density of synaptic boutons for axonal length, the probability of finding a connected postsynaptic interneuron is lower. Nevertheless, it is quite intriguing to observe that out of 5 recorded uEPSP, 4 showed amplitudes of several millivolts (reaching >5 mV responses in single

sweeps). This suggests that only few CR cells are required to control the activity of postsynaptic interneurons, and explains the powerful disynaptic GABAergic input observed onto pyramidal cells following CR cell optogenetic stimulation (Quattrocolo and Maccaferri 2014). In addition, these data prove unequivocally the glutamatergic nature of CR cells. This is important because the use of reelin expression as a CR cell-specific marker (in the absence of any other specific morphological/physiological characteristics) has generated severe misinterpretations of experimental results in the postnatal hippocampus (Yu et al. 2014), due to the presence of reelin-expressing GABAergic interneurons (for example, neurogliaform cells, see review, by Armstrong et al. 2012).

Conclusions

In summary, our findings reveal that CR are an integral part of the developing and mature hippocampal formation, and thus contribute importantly both to its local and long distance excitatory synaptic connectivity. Although the postsynaptic targets (i.e., GABAergic, excitatory neurons, or both) of CR cell at distant regions remain to be determined in more detail, the presence of another excitatory loop within the hippocampal formation is likely to add a new level of instability potentially supporting epileptiform activity. Indeed, it is intriguing that CR cell numbers in the hippocampal formation of patients suffering from temporal lobe epilepsy are increased (Blümcke et al. 1999). Whether this should be regarded as a causal factor that contributes to seizures because of direct excitatory output onto glutamatergic neurons versus a plastic response attempting to increase excitatory drive to GABAergic neurons remains to be determined.

Funding

This work was supported by the National Institutes of Health (grant NS064135 to G.M.). Funding to pay the Open Access publication charges for this article was provided by the Research Centre Jülich GmbH.

Notes

The excellent technical assistance of Ulrike Bandelow and Sun-Kyong Lee is very much appreciated. We thank the UKE Microscopy Imaging Facility under Dr Antonio Virgilio Failla for their excellent technical support with the Leica SP5 confocal microscope. We further thank Christina Greven for helpful comments and critical reading a preliminary version of the manuscript. We also thank Mike Fiske for reading the manuscript and providing valuable comments. *Conflict of Interest*: The authors declare no competing financial interests.

References

Abraham H, Meyer G. 2003. Reelin-expressing neurons in the postnatal and adult human hippocampal formation. Hippocampus. 13:715–727.

Abraham H, Perez-Garcia CG, Meyer G. 2004. p73 and Reelin in Cajal-Retzius cells of the developing human hippocampal formation. Cereb Cortex. 14:484–495.

Alcántara S, Ruiz M, D'Arcangelo G, Ezan F, de Lecea L, Curran T, Sotelo C, Soriano E. 1998. Regional and cellular patterns of reelin mRNA expression in the forebrain of the developing and adult mouse. J Neurosci. 18:7779–7799.

Ali AB, Thomson AM. 1998. Facilitating pyramid to horizontal oriens-alveus interneurone inputs: dual intracellular recordings in slices of rat hippocampus. J Physiol. 507:185–199.

Andersen P, Holmqvist B, Voorhoeve PE. 1966. Entorhinal activation of dentate granule cells. Acta Physiol Scand. 66:448–460.

Anstötz M, Cosgrove KE, Hack I, Mugnaini E, Maccaferri G, Lübke JHR. 2014. Morphology, input-output relations and synaptic connectivity of Cajal-Retzius cells in layer 1 of the developing neocortex of CXCR4-EGFP mice. Brain Struct Funct. 219:2119–2139.

Armstrong C, Krook-Magnuson E, Soltesz I. 2012. Neurogliaform and ivy cells: a major family of nNOS Expressing GABAergic neurons. Front Neural Circuits. 6:23.

Bhattacharyya BJ, Banisadr G, Jung H, Ren D, Cronshaw DG, Zou Y, Miller RJ. 2008. The chemokine stromal cell-derived factor-1 regulates GABAergic inputs to neural progenitors in the postnatal dentate gyrus. J Neurosci. 28:6720–6730.

Bielle F, Griveau A, Narboux-Nême N, Vigneau S, Sigrist M, Arber S, Wassef M, Pierani A. 2005. Multiple origins of Cajal-Retzius cells at the borders of the developing pallium. Nat Neurosci. 8:1002–1012.

Blümcke I, Beck H, Suter B, Hoffmann D, Födisch HJ, Wolf HK, Schramm J, Elger CE, Wiestler OD. 1999. An increase of hippocampal calretinin-immunoreactive neurons correlates with early febrile seizures in temporal lobe epilepsy. Acta Neuropathol. 97:31–39.

Boccara CN, Sargolini F, Thoresen VH, Solstad T, Witter MP, Moser EI, Moser MB. 2010. Grid cells in pre- and parasubiculum. Nat Neurosci. 13:987–994.

Bonnevie T, Dunn B, Fyhn M, Hafting T, Derdikman D, Kubie JL, Roudi Y, Moser EI, Moser MB. 2013. Grid cells require excitatory drive from the hippocampus. Nat Neurosci. 16:309–317.

Ceranik K, Bender R, Geiger JR, Monyer H, Jonas P, Frotscher M, Lübke J. 1997. A novel type of GABAergic interneuron connecting the input and the output regions of the hippocampus. J Neurosci. 17:5380–15394.

Ceranik K, Deng J, Heimrich B, Lübke J, Zhao S, Förster E, Frotscher M. 1999. Hippocampal Cajal-Retzius cells project to the entorhinal cortex: retrograde tracing and intracellular labelling studies. Eur J Neurosci. 11:4278–4290.

Ceranik K, Zhao S, Frotscher M. 2000. Development of the entorhino-hippocampal projection: guidance by Cajal-Retzius cell axons. Ann N Y Acad Sci. 911:43–54.

Chowdhury TG, Jimenez JC, Bomar JM, Cruz-Martin A, Cantle JP, Portera-Cailliau C. 2010. Fate of Cajal-Retzius neurons in te postnatal mouse cortex. Front Neuroanat. 4:10.

Cline H, Haas K. 2008. The regulation of dendritic arbor development and plasticity by glutamatergic synaptic input: a review of the synaptotrophic hypothesis. J Physiol. 586:1509–1517.

D'Arcangelo G, Miao GG, Chen SC, Soares HD, Morgan JI, Curran T. 1995. A protein related to extracellular matrix proteins deleted in the mouse mutant reeler. Nature. 374:719–723.

Del Río JA, Heimrich B, Borrell V, Förster E, Drakew A, Alcántara S, Nakajima K, Miyata T, Ogawa M, Mikoshiba K, et al. 1997. A role for Cajal-Retzius cells and reelin in the development of hippocampal connections. Nature. 385:70–74.

Derer P, Derer M, Goffinet A. 2001. Axonal secretion of Reelin by Cajal-Retzius cells: evidence from comparison of normal and Reln(Orl) mutant mice. J Comp Neurol. 440:136–143.

Drakew A, Frotscher M, Deller T, Ogawa M, Heimrich B. 1998. Developmental distribution of a reeler gene-related antigen in the rat hippocampal formation visualized by CR-50 immunocytochemistry. Neuroscience. 82:1079–1086.

Feldmeyer D, Egger V, Lübke J, Sakmann B. 1999. Reliable synaptic connections between pairs of excitatory layer 4 neurones within a single "barrel" of developing rat somatosensory cortex. J Physiol. 521:169–190.

Feldmeyer D, Lübke J, Sakmann B. 2006. Efficacy and connectivity of intracolumnar pairs of layer 2/3 pyramidal cells in the barrel cortex of juvenile rats. J Physiol. 575:583–602.
Frotscher M. 1998. Cajal-Retzius cells, Reelin, and the formation of layers. Curr Opin Neurobiol. 8:570–575.
Gu X, Liu B, Wu X, Yan Y, Zhang Y, Wei Y, Pleasure SJ, Zhao C. 2011. Inducible genetic lineage tracing of cortical hem derived Cajal-Retzius cells reveals novel properties. PLoS One. 6:e28653.
Gu X, Yan Y, Li H, He D, Pleasure SJ, Zhao C. 2009. Characterization of the Frizzled10-CreER transgenic mouse: an inducible Cre line for the study of Cajal-Retzius cell development. Genesis. 47:210–216.
Hafting T, Fyhn M, Molden S, Moser MB, Moser EL. 2005. Microstructure of a spatial map in the entorhinal cortex. Nature. 436:801–806.
Ina A, Sugiyama M, Konno J, Yoshida S, Ohmomo H, Nogami H, Shutoh F, Hisano S. 2007. Cajal-Retzius cells and subplate neurons differentially express vesicular glutamate transporters 1 and 2 during development of mouse cortex. Eur J Neurosci. 26:615–623.
Kilb W, Luhmann HJ. 2000. Characterization of a hyperpolarization-activated inward current in Cajal-Retzius cells in rat neonatal neocortex. J Neurophysiol. 84:1681–1691.
Kitamura T, Pignatelli M, Suh J, Kohara K, Yoshiki A, Abe K, Tonegawa S. 2014. Island cells control temporal association memory. Science. 343:896–890.
Kwon HB, Sabatini BL. 2011. Glutamate induces de novo growth of functional spines in developing cortex. Nature. 474:100–104.
Langston RF, Ainge JA, Couey JJ, Canto CB, Bjerknes TL, Witter MP, Moser EL, Moser MB. 2010. Development of the spatial representation system in the rat. Science. 328:1576–1580.
Marchionni I, Beaumont M, Maccaferri G. 2012. The chemokine CXCL12 and the HIV-1 envelope protein gp120 regulate spontaneous activity of Cajal-Retzius cells in opposite directions. J Physiol. 590:3185–3202.
Marchionni I, Maccaferri G. 2009. Quantitative dynamics and spatial profile of perisomatic GABAergic input during epileptiform synchronization in the CA1 hippocampus. J Physiol. 587:5691–5708.
Marchionni I, Takács VT, Nunzi MG, Mugnaini E, Miller RJ, Maccaferri G. 2010. Distinctive properties of CXC chemokine receptor 4-expressing Cajal-Retzius cells versus GABAergic interneurons of the postnatal hippocampus. J Physiol. 588:2859–2878.
Markram H, Lübke J, Frotscher M, Roth A, Sakmann B. 1997. Physiology and anatomy of synaptic connections between thick tufted pyramidal neurones in the developing rat neocortex. J Physiol. 500:409–440.
Megías M, Emri Z, Freund TF, Gulyás AI. 2001. Total number and distribution of inhibitory and excitatory synapses on hippocampal CA1 pyramidal cells. Neuroscience. 102:527–540.
Meyer G, Cabrera Socorro A, Perez Garcia CG, Martinez Millan L, Walker N, Caput D. 2004. Developmental roles of p73 in Cajal-Retzius cells and cortical patterning. J Neurosci. 24:9878–9887.
Moser EI, Kropff E, Moser MB. 2008. Place cells, grid cells, and the brain's spatial representation system. Ann Rev Neurosci. 31:69–89.
Ogawa M, Miyata T, Nakajima K, Yagyu K, Seike M, Ikenaka K, Yamamoto H, Mikoshiba K. 1995. The reeler gene-associated antigen on Cajal-Retzius neurons is a crucial molecule for laminar organization of cortical neurons. Neuron. 14:899–912.
O'Keefe J, Dostrovsky J. 1971. The hippocampus as a spatial map. Preliminary evidence from unit activity in the freely-moving rat. Brain Res. 34:171–175.
Oppenheim RW, Flavell RA, Vinsant S, Prevette D, Kuan CY, Rakic P. 2001. Programmed cell death of developing mammalian neurons after genetic deletion of caspases. J Neurosci. 21:4752–4760.
Pesold C, Impagnatiello F, Pisu MG, Uzunov DP, Costa E, Guidotti A, Caruncho HJ. 1998. Reelin is preferentially expressed in neurons synthesizing gamma-aminobutyric acid in cortex and hippocampus of adult rats. Proc Natl Acad Sci USA. 95:3221–3226.
Pesold C, Liu WS, Guidotti A, Costa E, Caruncho HJ. 1999. Cortical bitufted, horizontal, and Martinotti cells preferentially express and secrete reelin into perineuronal nets, nonsynaptically modulating gene expression. Proc Natl Acad Sci USA. 96:3217–3222.
Quattrocolo G, Maccaferri G. 2013. Novel GABAergic circuits mediating excitation/inhibition of Cajal-Retzius cells in the developing hippocampus. J Neurosci. 33:5486–5498.
Quattrocolo G, Maccaferri G. 2014. Optogenetic activation of Cajal-Retzius cells reveals their glutamatergic output and a novel feedforward circuit in the developing mouse hippocampus. J Neurosci. 34:13018–13032.
Radnikow G, Feldmeyer D, Lübke J. 2002. Axonal projection, input and output synapses, and synaptic physiology of Cajal-Retzius cells in the developing rat neocortex. J Neurosci. 22:6908–6919.
Ranck JB Jr. 1973. Studies on single neurons in dorsal hippocampal formation and septum in unrestrained rats. I. Behavioral correlates and firing repertoires. Exp Neurol. 41:461–531.
Sava BA, Dávid CS, Teissier A, Pierani A, Staiger JF, Luhmann HJ, Kilb W. 2010. Electrophysiological and morphological properties of Cajal-Retzius cells with different ontogenetic origins. Neuroscience. 167:724–734.
Sik A, Ylinen A, Penttonen M, Buzsáki G. 1994. Inhibitory CA1-CA3-hilar region feedback in the hippocampus. Science. 265:1722–1724.
Soda T, Nakashima R, Watanabe D, Nakajima K, Pastan I, Nakanishi S. 2003. Segregation and coactivation of developing neocortical layer 1 neurons. J Neurosci. 23:6272–6279.
Soriano E, Del Río JA. 2005. The cells of Cajal-Retzius: still a mystery one century after. Neuron. 46:389–394.
Steward O, Scoville SA. 1976. Cells of origin of entorhinal cortical afferents to the hippocampus and fascia dentata of the rat. J Comp Neurol. 169:347–370.
Supèr H, Martínez A, Del Río JA, Soriano E. 1998. Involvement of distinct pioneer neurons in the formation of layer-specific connections in the hippocampus. J Neurosci. 18:4616–4626.
Takiguchi-Hayashi K, Sekiguchi M, Ashigaki S, Takamatsu M, Hasegawa H, Suzuki-Migishima R, Yokoyama M, Nakanishi S, Tanabe Y. 2004. Generation of reelin-positive marginal zone cells from the caudomedial wall of telencephalic vesicles. J Neurosci. 24:2286–2295.
Tissir F, Ravni A, Achouri Y, Riethmacher D, Meyer G, Goffinet AM. 2009. DeltaNp73 regulates neuronal survival in vivo. Proc Natl Acad Sci USA. 106:16871–16876.
Wills TJ, Barry C, Cacucci F. 2012. The abrupt development of adult-like grid cell firing in the medial entorhinal cortex. Front Neural Circuits. 6:21.
Wills TJ, Cacucci F, Burgess N, O'Keefe J. 2010. Development of the hippocampal cognitive map in preweanling rats. Science. 328:1573–1576.
Yoshida M, Assimacopoulos S, Jones KR, Grove EA. 2006. Massive loss of Cajal-Retzius cells does not disrupt neocortical layer order. Development. 133:537–545.
Yu D, Fan W, Wu P, Deng J, Liu J, Niu Y, Li M, Deng J. 2014. Characterization of hippocampal Cajal-Retzius cells during development in a mouse model of Alzheimer's disease (Tg2576). Neural Regen Res. 9:394–401.